# A General 3-D Nonstationary GBSM for Underground Vehicular Channels

Hengtai Chang, *Member, IEEE*, Cheng-Xiang Wang, *Fellow, IEEE*, Yu Liu, *Member, IEEE*, Jie Huang, *Member, IEEE*, Jian Sun, *Member, IEEE*, Wensheng Zhang, *Member, IEEE*, Zhiquan Bai, *Senior Member, IEEE*, Kang An, Zengliang Li, and El-Hadi M. Aggoune, *Life Senior Member, IEEE*

***Abstract*— Reliable and efficient communications are indispensable for vehicles in underground environments. Underground wireless channels present a number of unique properties, such as guided propagation, rich scatterers, and near-field/far-field effect. In this article, a 3-D twin cluster geometry-based stochastic model (GBSM) is proposed to describe underground vehicular channel characteristics in both pillar and tunnel scenarios. The proposed model supports arbitrary trajectory mobility of vehicles and multiple antenna configurations at the transmitter (Tx) and the receiver (Rx). The cluster time evolution is modeled by different scatterer generation and updating methods to simulate the channel characteristics such as nonstationarity, near-field/far-field differences, and waveguide effects. Based on the proposed channel model, the statistical characteristics of the channel are derived and simulated, including the temporal autocorrelation function (ACF), spatial cross-correlation function (CCF), delay power spectrum density (PSD), Doppler PSD, and so on. Besides, underground channel measurements at 2.5/3.5 GHz are conducted in a garage scenario. Comparison results of channel measurements and simulations validate the accuracy and usefulness of the proposed GBSM.**

***Index Terms*— Communication channels, electromagnetic propagation, radio propagation, time-varying channels.**

Manuscript received 9 July 2021; revised 19 September 2022; accepted 23 November 2022. Date of publication 29 December 2022; date of current version 3 February 2023. This work was supported in part by the National Key Research and Development Program of China under Grant 2018YFB1801101; in part by the National Natural Science Foundation of China (NSFC) under Grant 61960206006, Grant 61771291, Grant 62071276, and Grant 62001269; in part by the Key Technologies Research and Development Program of Jiangsu (Prospective and Key Technologies for Industry) under Grant BE2022067, Grant BE2022067-1, and Grant BE2022067-3; in part by the Research Fund of National Mobile Communications Research Laboratory, Southeast University, under Grant 2021B02; in part by the EU H2020 RISE TESTBED2 Project under Grant 872172; in part by the Distinguished Postdoctoral Program in Jiangsu; in part by the Taishan Scholar Program of Shandong Province; in part by the Shandong Provincial Natural Science Foundation under Grant ZR2019BF04, Grant ZR2020MF002, and Grant ZR2021LZH003; in part by the Fundamental Research Funds of Shandong University under Grant 2020GN032; and in part by the University of Tabuk, Saudi Arabia, under Grant S-1443-001. *(Corresponding author: Cheng-Xiang Wang.)*

Hengtai Chang is with the Purple Mountain Laboratories, Nanjing 211111, China, and also with the School of Information Science and Engineering, Southeast University, Nanjing 210096, China (e-mail: changhengtai@pmlabs.com.cn).

Cheng-Xiang Wang and Jie Huang are with the National Mobile Communications Research Laboratory, School of Information Science and Engineering, Southeast University, Nanjing 210096, China, and also with the Purple Mountain Laboratories, Nanjing 211111, China (e-mail: chxwang@seu.edu.cn; j_huang@seu.edu.cn).

Yu Liu is with the School of Microelectronics, Shandong University, Jinan 250101, China (e-mail: yuliu@sdu.edu.cn).

Jian Sun, Wensheng Zhang, and Zhiquan Bai are with the Shandong Provincial Key Laboratory of Wireless Communication Technologies, School of Information Science and Engineering, Shandong University, Qingdao 266237, China (e-mail: sunjian@sdu.edu.cn; zhangwsh@sdu.edu.cn; zqbai@sdu.edu.cn).

Kang An and Zengliang Li are with the Innovation and Research Institute of HIWING Technology Academy, Fengtai, Beijing 100074, China (e-mail: kangan@buaa.edu.cn; lzl811@163.com).

El-Hadi M. Aggoune is with the Sensor Networks and Cellular Systems Research Center, University of Tabuk, Tabuk 47315/4031, Saudi Arabia (e-mail: hadi.aggoune@gmail.com).

Color versions of one or more figures in this article are available at https://doi.org/10.1109/TAP.2022.3231679.

Digital Object Identifier 10.1109/TAP.2022.3231679

## I. Introduction

RECENTLY, the development of underground space is increasing, and the applications of underground facilities are diversifying. Due to the ground obstruction and complex underground environment, the existing mobile communication system usually cannot cover the underground space [1], [2], which requires the design and implementation of underground communication systems to ensure the full scenario coverage of next-generation wireless networks [3], [4]. Specifically, the underground vehicular communication is indispensable for underground navigation, vehicle collaboration, and realization of the intelligent transportation system (ITS). Besides, in the underground exploration and sensing, employing unmanned vehicles, including unmanned ground vehicles (UGVs), and unmanned aerial vehicles (UAVs), can be a significant solution due to their convenience and security. Reliable unmanned vehicles to unmanned vehicles and unmanned vehicles to background control center communications can ensure the accomplishment of tasks. Underground space is a kind of enclosed space, where the propagation characteristics of electromagnetic waves are different from open space. The channel model that can capture the unique characteristics of the underground vehicular channel is essential for communication system design and will play an important role in link budget, transmission scheme selection, and system performance evaluation [5], [6], [7].

For the special environment of underground space, a lot of wireless channel-related studies have been conducted based on the channel measurement, simulation, and theoretical analysis. Depending on the function of underground facilities, underground space can be divided into underground garages, tunnels, subways, mines, and so on. For the underground garage scenario, the Aalborg University research team developed a large-scale fading channel model based on the $\alpha - \beta$ model [8], which also took into account the signal loss between multistory garages based on 800 MHz and 2 GHz channel measurements. The University of South Carolina Team proposed a nongeometric stochastic channel model based on the tap-delay-line (TDL) structure [9], which supports both line-of-sight (LoS) and nonLoS (NLoS) conditions based on channel measurement at 5 GHz. Besides, the path loss model and multipath model were established based on ultrawideband channel measurements (3.28–5.03 GHz) in the underground garage scenario at Korea Dong International University [10], [11]. Beijing Jiaotong University conducted channel measurement at 5.9 GHz in the garage scenario, and antenna array was used in the measurement to obtain the directional characteristics of the channel [12].

For the subway scenario, Lienard et al. [13] conducted channel measurements in the 900 MHz band for a metro tunnel scenario using the channel sounder. The effects of tunnel narrowing, bending, and sheltering on the channel were investigated through the analysis of parameters such as path loss and delay spread, and the feasibility of using multiple-input multiple-output (MIMO) to increase the channel capacity in tunnel scenarios was discussed [14]. Valdesueiro et al. [15] conducted channel measurements in the 5.8 GHz band, using software-defined radio equipment at both the transmitter (Tx) and the receiver (Rx) and investigated channel capacity, as well as the tradeoff between antenna spacing and diversity gain for $2 \times 2$ MIMO systems. Zhang et al. [16] combined vector parabolic equations with waveguide mode theory to model subway tunnel scenarios in the 1 and 2 GHz frequency bands. The influence of operating frequency and tunnel section shape on the signal propagation characteristics was investigated based on the parametric analysis of the received power, fading statistics, and path loss probability distribution [16]. Guan et al. [17] measured and computed propagation characteristics of a subway environment at 2.4 GHz, including near shadowing, path loss, and shadow fading.

For the tunnel scenario, Valdesueiro et al. [18] performed channel measurements at 2.6 GHz with a bandwidth of 10 MHz using a measurement platform based on the universal software radio peripheral (USRP) B210 to analyze path loss, time delay, and Doppler spread. The [19] conducted vehicle-to-vehicle (V2V) channel measurements in an arched tunnel in Madrid, using the multiple-input single-output (MISO) antenna fixed on the train. Briso-Rodruez et al. [20] measured path loss and other large-scale fading parameters in an arched train tunnel at 900 MHz to develop a large-scale fading statistical channel model. Molina-Garcia-Pardo et al. [21] conducted channel measurements in a semicircular tunnel at 2.8–5 GHz and collected parameters such as path loss, the received signal amplitude probability density function (PDF), and the cumulative distribution function (CDF) with MIMO configuration. Qiu et al. [22] proposed an emulation TDL model for railway tunnels, considering the impact of the rolling stock.

For the mine scenario, Chehri et al. [23], [24], [25] conducted a series of measurements in the experimental mine located in Waldorf, Canada. The measurement campaign focused on ultrawideband channels at 2–5 GHz. In order to investigate the channel spatial variation, the Tx antenna was moved on a rectangular with $8 \times 5$ grids spaced 7 cm apart and the Rx antenna was fixed during the measurement. This reveals the large/small-scale fading and some frequency- and space-domain characteristics in the LoS and NLoS conditions. Sun and Akyildiz [26] proposed a multimode waveguide model that can characterize the fast fluctuations of the channel and give analytical expressions for the received power and channel impulse response (CIR) at arbitrary locations in the roadway. Based on this model, the authors investigated the effects of tunnel size, operating frequency, antenna position, and polarization. Linard and Degauque [27] and Ranjan et al. [28] proposed a hybrid multimode model combining waveguide and geometric-optical models to investigate the effects of surface roughness and mine wall tilt on the path loss.

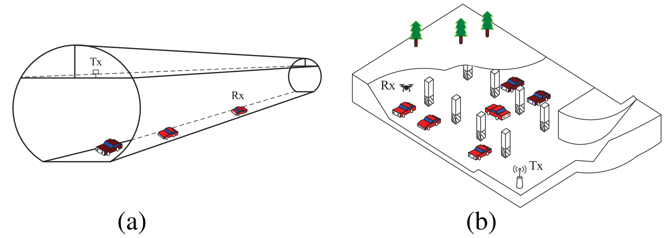


Fig. 1. Typical underground structures. (a) Tunnel structure. (b) Pillar structure.

Generally, the channel characteristics of underground space mainly depend on the spatial structure of the underground scenarios [29]. According to the different underground spatial structures, the underground space scenarios can be roughly divided into two types, that is, tunnel type and pillar type, as shown in Fig. 1. The tunnel structure scenarios contain subway tunnels, train tunnels, highway tunnels, mine roadways, and some other scenarios, in which the electromagnetic waves will be reflected between the walls many times to form the guided propagation. The pillar structure scenarios usually contain underground garage and pit face of mine, which have rich scatterers, for example, support pillars and parked vehicles. For clarity, significant channel properties in tunnel and pillar scenarios are listed in Table I. The existing researches on underground space channel mainly focus on exploring and analyzing the channel characteristics of different scenarios and lack a common channel model for different structure scenarios. The development of a general underground channel model supporting different underground structures and transceiver moving modes are indispensable for underground propagation mechanism simulation, which is very important to the Antennas and Propagation Community.

This article addresses the problem of nonstationary underground channel modeling. The proposed underground channel model is applicable to both tunnel and pillar scenarios and can support arbitrary trajectory mobility of vehicles, as well as multiple antenna configurations. Compared with previous works modeling underground channels [8], [9], [10], [11], [12], [13], [14], [15], [16], [17], [18], [19], [20], [21], [22], [23], [24], [25], [26], [27], [28] and open space vehicular and UAV channels [30], [31], [32], [33], [34], [35], the contributions and innovations of this article are summarized as follows.

1) A general nonstationary geometry-based stochastic model (GBSM) is proposed for two types of underground vehicular channels (tunnel scenario and pillar scenario) by considering different channel characteristics

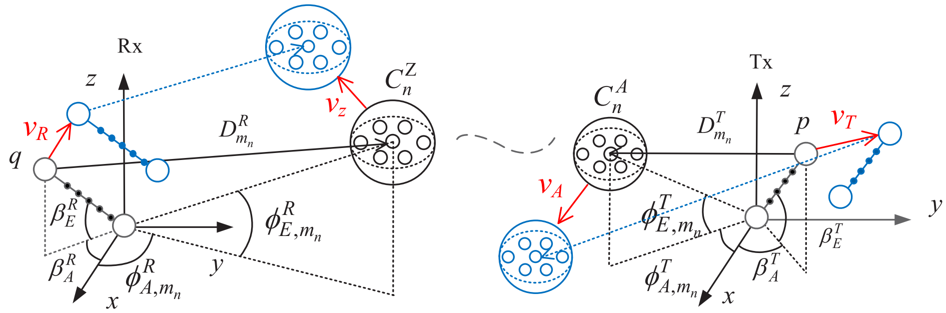


Fig. 2. 3-D wideband twin cluster channel model framework.

TABLE I
CHANNEL PROPERTIES IN UNDERGROUND SCENARIOS

| | Waveguide/cluster/scatterer properties |
|---|---|
| Tunnel | Obvious waveguide effect |
| | Near-field/far-field channel difference |
| | Aperture effect lead to convergent clusters parameters |
| Pillar | Non-obvious waveguide effect |
| | MPCs mainly come from near scatterers |
| | The clutter distribution of scatterers in enclosed space |

brought by different underground structure scenarios, including waveguide effect, near/far-field effect, and the enclosed property of underground space.

2) Channel statistical properties of the proposed underground channel model, including delay/angular/Doppler power spectrum density (PSD), the space–time–frequency correlation function (STF-CF), level-cross rate (LCR), average fading duration (AFD), and stationary interval, are thoroughly derived and simulated. Vehicular MIMO channel characteristics in different underground scenarios are compared through simulation results.

3) Underground channel measurements are conducted at 2.5/3.5 GHz and some simulation parameters are obtained by fitting measurement data. The measurement results are compared with simulation results, validating the accuracy and usefulness of the proposed channel model.

The rest of this article is organized as follows. In Section II, the geometry construction and parameter generation methods of the proposed channel model are described. In Section III, derivations of statistical properties such as delay PSD, STF-CF, LCR, and AFD are provided. In Section IV, channel simulation results in different underground scenarios are analyzed. Channel model validation through channel measurement is provided in Section V. Conclusions are drawn in Section VI.

## II. 3-D WIDEBAND UNDERGROUND MIMO GBSM

The underground space usually has abundant scatterers and enclosed space. Multibounce multipath components (MPCs) account for a considerable proportion in the whole CIR. In this case, the application of the general geometric stochastic modeling method or ray-tracing method to generate the MPCs will lead to unnecessary computation [36]. To address this problem, the twin cluster modeling framework abstracting the propagation between the first and last bounce as a virtual link can reduce the computation and improve the simulation efficiency greatly [37], [41]. Furthermore, to characterize different channel properties in tunnel or pillar scenarios, based on the twin cluster model framework, we fine two different ways to generate and update the cluster level parameters. Channel properties are reflected in generation of the simulation parameters, which ensures the generality of the proposed model.

The twin cluster model is shown schematically in Fig. 2, and the key parameters involved in the proposed model are listed in Table II. Considering that electromagnetic wave propagation in underground scenarios will experience large- and small-scale fading, the MIMO wideband fading channels can be represented by CIR matrix

$$\mathbf{H} = [PL \cdot SH]^{1/2} \cdot \mathbf{H}_s \tag{1}$$

where $PL$ is the path loss caused by propagation distance between the Tx and Rx. Shadowing is represented by $SH$. Matrix $\mathbf{H}_s$ represents small-scale fading. Due to different path loss exponent at near-field and far-field in underground scenario, we use two-slope large-scale fading model, that is,

$$PL = \begin{cases} A_1 + n_1 10\log_{10}(d), & \text{if } d \le r_{bp} \\ B_1 + n_2 10\log_{10}(d), & \text{if } d > r_{bp} \end{cases} \tag{2}$$

where $d$ is the distance between Tx and Rx, $r_{bp}$ is the break point dividing the near-field and far-field, and usually takes the value of $r_{bp} = \max\{w^2/\lambda, h^2/\lambda\}$, where $w$ and $h$ are cross-sectional dimensions. Parameters $A_1$, $A_2$, $n_1$, and $n_2$ can be obtained by channel measurement or simulation. Note that the break point not only separates near/far fields with different large-scale fading properties in waveguide transmission, but also separates near/far fields with different small-scale fading properties [29].

Small-scale channel fading is resulted from multipath propagation caused by objects and walls in underground space. A typical 3-D MIMO channel between Tx having $n_T$ antenna elements and Rx having $n_R$ antenna elements is illustrated in Fig. 2. Scatterers in the real world are abstracted as a number of scattering clusters. For the sake of simplicity, only the $n$th cluster is presented in figure. Meanwhile, the first and last bounce clusters are represented by sphere beside Tx, $C^A_n$, and sphere beside Rx, $C^Z_n$, respectively. The propagation path between $C^A_n$ and $C^Z_n$ can be denoted as a virtual link having a randomly generated delay. Besides, when a path propagates through single bounce, the delay of the virtual link will be zero. This channel modeling framework supports mobility of Tx, Rx, $C_n^A$, and $C_n^Z$, that is, time-variant coordinates $\vec{A}_0^T$, $\vec{A}_0^R$, $\vec{C}_n^A$, and $\vec{C}_n^Z$. Let $\phi_{A,m_n}^T$ and $\phi_{E,m_n}^T$ denote the azimuth and elevation angles of departure (AAoD/EAoD) of the $m$th ray in cluster $C_n^A$, respectively. Let $\phi_{A,m_n}^R$ and $\phi_{E,m_n}^R$ denote azimuth and elevation angles of arrival (AAoA/EAoA) of the $m$th ray in cluster $C_n^Z$. Similarly, let $\phi_{A,\mathrm{LoS}}^T$, $\phi_{E,\mathrm{LoS}}^T$, $\phi_{A,\mathrm{LoS}}^R$, and $\phi_{E,\mathrm{LoS}}^R$ stand for the AAoD, EAoD, AAoA, and EAoA of the LoS path, respectively.

The small-scale fading of the wideband MIMO channel can be described as a matrix $\mathbf{H}_s = [h_{pq}(t,\tau)]_{n_T \times n_R}$. The entries of $\mathbf{H}_s$ consist of two components, that is, the LoS and NLoS components, and is written as

$$h_{pq}(t,\tau) = \sqrt{\frac{K_R}{K_R+1}} h_{pq}^{\mathrm{LoS}}(t,\tau) + \sqrt{\frac{1}{K_R+1}} h_{pq}^{\mathrm{NLoS}}(t,\tau) \quad (3)$$

where $K_R$ is the Ricean $K$-factor. The NLoS components $h_{pq}^{\mathrm{NLoS}}(t,\tau)$ is written as

$$\begin{aligned} h_{pq}^{\mathrm{NLoS}}&(t,\tau) \\ &= \sum_{n=1}^{N(t)} \sum_{m=1}^{M_n} \begin{bmatrix} F_{q,V}\left(\phi_{E,m_n}^R, \phi_{A,m_n}^R\right) \\ F_{q,H}\left(\phi_{E,m_n}^R, \phi_{A,m_n}^R\right) \end{bmatrix}^T \\ &\quad \times \begin{bmatrix} e^{j\theta_{mn}^{VV}} & \sqrt{\kappa_{m_n}^{-1}} e^{j\theta_{mn}^{VH}} \\ \sqrt{\kappa_{m_n}^{-1}} e^{j\theta_{mn}^{HV}} & e^{j\theta_{mn}^{HH}} \end{bmatrix} \begin{bmatrix} F_{p,V}\left(\phi_{E,m_n}^T, \phi_{A,m_n}^T\right) \\ F_{p,H}\left(\phi_{E,m_n}^T, \phi_{A,m_n}^T\right) \end{bmatrix} \\ &\quad \cdot \sqrt{P_{pq,m_n}(t)} \cdot e^{j2\pi f_c \tau_{pq,m_n}(t)} \cdot \delta\left(\tau - \tau_{pq,m_n}(t)\right) \end{aligned} \quad (4)$$

where $\{\cdot\}^T$ represents transposition, and $f_c$ denotes the carrier central frequency. Functions $F_{p,V/H}$ and $F_{q,V/H}$ are the antenna patterns of Tx and Rx, the superscripts $V$ and $H$ denote vertical polarization and horizontal polarization, respectively. Besides, $\kappa_{m_n}$ denotes the cross polarization power ratio, $\theta_{m_n}^{VV}$, $\theta_{m_n}^{VH}$, $\theta_{m_n}^{HV}$, and $\theta_{m_n}^{HH}$ denote the random phases uniformly distributed within $(0, 2\pi]$, $P_{pq,m_n}(t)$ and $\tau_{pq,m_n}(t)$ are the normalized power and delay of the $m$th ray in the $n$th cluster at time $t$, respectively. For the LoS component, it can be written as

$$\begin{aligned} h_{pq}^{\mathrm{LoS}}(t,\tau) &= \begin{bmatrix} F_{q,V}\left(\phi_{E,\mathrm{LoS}}^R, \phi_{A,\mathrm{LoS}}^R\right) \\ F_{q,H}\left(\phi_{E,\mathrm{LoS}}^R, \phi_{A,\mathrm{LoS}}^R\right) \end{bmatrix}^T \begin{bmatrix} e^{j\theta_{\mathrm{LoS}}^{VV}} & 0 \\ 0 & e^{j\theta_{\mathrm{LoS}}^{HH}} \end{bmatrix} \\ &\quad \times \begin{bmatrix} F_{p,V}\left(\phi_{E,\mathrm{LoS}}^T, \phi_{A,\mathrm{LoS}}^T\right) \\ F_{p,H}\left(\phi_{E,\mathrm{LoS}}^T, \phi_{A,\mathrm{LoS}}^T\right) \end{bmatrix} \\ &\quad \cdot e^{j2\pi f_c \tau_{pq,\mathrm{LoS}}(t)} \delta\left(\tau - \tau_{pq,\mathrm{LoS}}(t)\right) \end{aligned} \quad (5)$$

where $\theta_{\mathrm{LoS}}^{VV}$ and $\theta_{\mathrm{LoS}}^{HH}$ are random phases that uniformly distributed within $(0, 2\pi]$, and $\tau_{pq,\mathrm{LoS}}$ refer to the delay of LoS component.

In the proposed model, channel simulation parameters can be divided into two categories: 1) large-scale parameters (LSPs) including delay spread, Ricean K-factor, shadowing fading, and AAoA/ EAoA/AAoD/EAoD spreads generated in simulation initialization step and 2) small scale parameters (SSPs) including AAoAs, EAoAs, AAoDs, EAoDs, time delays, phases, and powers for different clusters, which will be generated or updated at each time instants [47].

The channel simulation process has two stages, that is, model initialization and time evolution. In the model initialization stage, the scenario types, antenna parameters, Tx/Rx trajectories, and LSPs are generated first. Then the initial scattering cluster parameters are generated according to the scenario structure type. For channel simulation process in tunnel and pillar scenarios, the detailed flowchart is presented in Fig. 3.

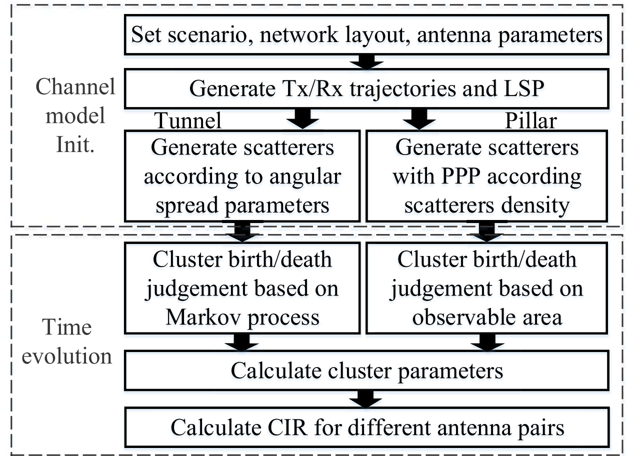


Fig. 3. Flowchart of the channel simulation process.

For the tunnel structure scenario, since the centrality of clusters in angular domain, the angle spread, cluster generation, and recombination rates are used to generate the scattering clusters concentrated in the tunnel trending direction. For the pillar scenario, since the randomness of scatterer distribution, the Poisson point process (PPP) is used to generate randomly distributed scattering clusters in the finite space.

Due to the motions of the Tx, Rx, and scatterers, the channel will present nonstationarity, that is, channel parameters vary with time. It means that channel parameters should be updated at each time instant during simulation. Based on the channel sampling theorem in [43], the time-variant channel can be divided into a series of segments by time interval $\Delta t_{\mathrm{BD}}$, and in each time interval the channel can be seen as constant. The maximum time interval can be determined according to Doppler bandwidth as

$$\Delta t_{\mathrm{BD}} \leq \frac{1}{2B_D} = \frac{\lambda}{4\max\left|\vec{v}_T - \vec{v}_R + \vec{v}_Z - \vec{v}_A\right|} \quad (6)$$

where $B_D$ is the width of the Doppler spectrum, and $\vec{v}_T$, $\vec{v}_R$, $\vec{v}_A$, and $\vec{v}_Z$ represent the vector of velocities at Tx, Rx, $C_n^A$, and $C_n^Z$. Since the open property of the tunnel scenario, MPCs from distant scatterers have considerable effect on channels, while in the pillar scenario, MPCs from distant scatterers will be obstructed by near scatterers. For each time interval, depending on scenario types, we implement the cluster birth/death algorithm based on the Markov process and the observable region and update the parameters of the surviving clusters to finally generate the corresponding CIR.

### *A. Cluster Generation and Time Evolution in Tunnel Scenario*

Considering the channel characteristics of the tunnel scenario and the demand of mobile communication between flexible moving vehicles, we use the channel parameter generation method and time evolution mechanism adapted to the corresponding channel characteristics. Specifically, we set different delay spread $\sigma_\tau$, angle spreads $AS(\phi_{A,m_n}^T/\phi_{E,m_n}^T/\phi_{A,m_n}^R/\phi_{E,m_n}^R)$,

TABLE II
DEFINITIONS OF MAIN PARAMETERS OF THE PROPOSED CHANNEL MODEL

| Symbol | Definition |
|---|---|
| $\vec{A}_0^T/\vec{A}_0^R$ | Position vectors of first transmit/receive antenna elements |
| $\vec{C}_n^A/\vec{C}_n^Z$ | Position vectors of clusters $C_n^A/C_n^Z$ |
| $\vec{C}_{m_n}^A/\vec{C}_{m_n}^Z$ | Position vectors of $m$-th ray in clusters $C_n^A/C_n^Z$ |
| $\beta_A^T/\beta_A^R$ | Azimuth angles of the transmit/receive antenna array broadside |
| $\beta_E^T/\beta_E^R$ | Elevation angles of the transmit/receive antenna array broadside |
| $\delta_T/\delta_R$ | Antenna spacings of the transmit/receive arrays |
| $\phi_{A,m_n}^T/\phi_{E,m_n}^T$ | Azimuth and elevation angles between $C_n^A$ and transmit antenna element via $m$-th ray |
| $\phi_{A,m_n}^R/\phi_{E,m_n}^R$ | Azimuth and elevation angles between $C_n^Z$ and receive antenna element via $m$-th ray |
| $\phi_{A,\mathrm{LoS}}^T/\phi_{E,\mathrm{LoS}}^T$ | AAoD and EAoD of the LoS component |
| $\phi_{A,\mathrm{LoS}}^R/\phi_{E,\mathrm{LoS}}^R$ | AAoA and EAoA of the LoS component |
| $D_n^T/D_n^R$ | Distances from transmit/receive to $C_n^A/C_n^Z$ |
| $D_{m_n}^R/D_{m_n}^T$ | Distances between transmit/receive antenna element and $C_n^A/C_n^Z$ via $m$-th ray |

and cluster birth/death control parameters $\lambda_{\mathrm{G}}(\lambda_{\mathrm{R}})$ for near-field and far-field according to whether the Tx–Rx distance is larger than break point distance $r_{bp}$. The temporal nonstationarity of the channel can be caused by the motion of the transceiver, and we introduce variable $\delta_P(t, \Delta t_{\mathrm{BD}})$ to describe the variation in the transmission environment from time $t$ to $t + \Delta t_{\mathrm{BD}}$. It represents the sum of the distances traveled by the Tx and Rx from time $t$ to $t + \Delta t_{\mathrm{BD}}$, that is,

$$\delta_P(t, \Delta t_{\mathrm{BD}}) = v_T(t)\Delta t_{\mathrm{BD}} + v_R(t)\Delta t_{\mathrm{BD}}. \tag{7}$$

Then, the probability of a cluster survived in this period can be represented by

$$P_{\mathrm{s}}(t, \Delta t_{\mathrm{BD}}) = \exp\left[-\lambda_R\left(\frac{\delta_p(t, \Delta t_{\mathrm{BD}})}{D_c}\right)\right] \tag{8}$$

where $D_c$ is a scenario-dependent coefficient controlling the spatial correlation. Typical values of $D_c$ can be chosen with the same order of correlation distance [37].

We consider all clusters having the same probability of survival. According to the definition of the Markov birth-death process, the clusters of a channel at moment $t + \Delta t_{\mathrm{BD}}$ are considered to be the sum of the clusters that survive from moment $t$ and the clusters that are generated at time intervals $\Delta t_{\mathrm{BD}}$. The birth and dead process is determined by cluster generation and recombination rates ($\lambda_G/\lambda_R$). Consequently, the mean value of the cluster number in the channel has the expression as

$$\mathbb{E}[N(t)] = \frac{\lambda_G}{\lambda_R}. \tag{9}$$

Based on the Markov birth death concept, the time interval between the creation and disappearance of the clusters follows an exponential distribution. The mean value of the number of new clusters can be expressed as

$$\mathbb{E}[N_{\mathrm{new}}(t + \Delta t_{\mathrm{BD}})] = \frac{\lambda_G}{\lambda_R}(1 - P_{\mathrm{s}}(t, \Delta t_{\mathrm{BD}})). \tag{10}$$

For each newly generated cluster, the 3-D coordinate of the cluster center are generated through the Tx/Rx near-field/far-field channel parameters, and due to the aperture effect in the tunnel scenario, the scattered clusters will usually be concentrated in the direction of the tunnel, and different angular spread can be used to characterize the spread of the scattered clusters in different regions. For the azimuth and elevation angles from the Rx to the center of the last bounce cluster, the angles can be expressed as

$$\phi_{A,n}^R = \mathrm{AS}(\phi_{A,n}^R)Y_{A,n}^R + \psi_{A,n}^R \tag{11}$$
$$\phi_{E,n}^R = \mathrm{AS}(\phi_{E,n}^R)Y_{E,n}^R + \psi_{E,n}^R \tag{12}$$

where $\mathrm{AS}(\phi_{A,n}^R)$ and $\mathrm{AS}(\phi_{E,n}^R)$ denote the azimuth and elevation angular spreads of the arrival angle, respectively, $Y_{A,n}^R$ and $Y_{E,n}^R$ follow the normal distribution $N(0, 1)$, and $\psi_{A,n}^R$ and $\psi_{E,n}^R$ denote the average of the azimuth and elevation angles, respectively. To determine the coordinate of the center of the last bounce scattering cluster with respect to (w.r.t.) to the Rx, a distance parameter is required according to scale of tunnel

$$D_n^R = \begin{cases} \dfrac{z - A_{0,z}^R}{\sin\phi_{E,n}^R} \\ \quad \text{if} \quad \dfrac{\tan\phi_{A,n}^R(z - A_{0,z}^R)}{\tan\phi_{E,n}^R} + A_{0,y}^R \in (y_{lw}, y_{rw}) \\ \dfrac{y - A_{0,y}^R}{\cos\phi_{A,n}^R \sin\phi_{E,n}^R} \\ \quad \text{if} \quad \dfrac{\tan\phi_{A,n}^R(z - A_{0,z}^R)}{\tan\phi_{E,n}^R} + A_{0,y}^R \notin (y_{lw}, y_{rw}) \end{cases} \tag{13}$$

where $A_{0,x}^R$, $A_{0,y}^R$, and $A_{0,z}^R$ are $x$, $y$, and $z$ components of the Rx coordinate, $y$ denotes the side wall of the tunnel, depending on $y = y_{lw}$ for the left side wall and $y = y_{rw}$ for the right side wall, and $z$ denotes the ceiling and bottom of the tunnel, depending on $z = z_t$ for ceiling and $z = z_b$ for bottom.

Similarly, the coordinates of the center of the first bounce scattering cluster with respect to the Tx can be obtained in the same way using the departure parameters azimuth and elevation angle spreads $\mathrm{AS}(\phi_{A,n}^R/\phi_{A,n}^R)$ and the distance parameter $D_n^T$. Subsequently, the 3-D coordinates of the scattering cluster and the center can be expressed as

$$\vec{C}_n^A = \vec{A}_0^T + \vec{D}_n^T \tag{14}$$
$$\vec{C}_n^Z = \vec{A}_0^R + \vec{D}_n^R \tag{15}$$

where $\vec{D}_n^T$ and $\vec{D}_n^R$ denote vectors from Tx/Rx to the scatterer center, that is,

$$\vec{D}_n^T = D_n^T \cdot \left[\cos\phi_{A,n}^T \cos\phi_{E,n}^T \quad \sin\phi_{A,n}^T \cos\phi_{E,n}^T \quad \sin\phi_{E,n}^T\right]^T$$
$$\vec{D}_n^R = D_n^R \cdot \left[\cos\phi_{A,n}^R \cos\phi_{E,n}^R \quad \sin\phi_{A,n}^R \cos\phi_{E,n}^R \quad \sin\phi_{E,n}^R\right]^T.$$

Finally, due to the spread of a scattering cluster in space, we use a 3-D Gaussian distribution to describe the dispersion of different scattering points in a scattering cluster, and for the $m$th subpath in the twin cluster $C_n^A$ and $C_n^Z$, the coordinates of the scattering points can be expressed as

$$\vec{C}_{m_n}^{A/Z} = \vec{C}_n^{A/Z} + \left[\Delta x_{m_n}^{A/Z} \quad \Delta y_{m_n}^{A/Z} \quad \Delta z_{m_n}^{A/Z}\right]^T \tag{16}$$

where $[\Delta x_{m_n}^{A/Z} \quad \Delta y_{m_n}^{A/Z} \quad \Delta z_{m_n}^{A/Z}]^T$ follows the 3-D Gaussian distribution with variance $\sigma_n^2$.

### *B. Cluster Generation and Time Evolution in the Pillar Scenario*

Considering that the scatterers in the pillar scenario are distributed in the finite space and usually are concentrated near the transceiver, we use a different approach to generate scattering clusters from the tunnel scenario. First, we use the PPP in finite space to generate the expected number of cluster centers in the underground space. The coordinates set of the cluster centers can be expressed by matrix $\mathbf{C}_{\text{tot}}=[\vec{C}_1 \quad \vec{C}_2 \quad \ldots \quad \vec{C}_{N_{\text{tot}}}]^T$, where $N_{\text{tot}}=$ Poisson$(\lambda_s L)$, and $\lambda_s$ and $L$ denote the scatterer density and volume of underground space. To generate the Poisson-distributed scatterer number, we use the stop time method [48]

$$N_{\text{tot}} = \max\left\{k \Big| \sum_{i=1}^{k} \log(U_i) < -\lambda_s L\right\} \tag{17}$$

where $U_i$ follows uniform distribution in (0,1). Due to the spread of each cluster in the pillar scenario, then we use (15) to generate the scattering points in each scattering cluster.

**Algorithm 1** Time Evolution in a Pillar Scenario

**Input**: $\vec{A}_0^T, \vec{A}_0^R, \mathbf{C}_{\text{tot}}, d_{\text{lim}}, N_{\text{tot}}$
**Output**: $\mathbf{C}_{\text{tot}}^{\text{A}}, \mathbf{C}_{\text{tot}}^{\text{Z}}$
**Initialize** $i = 0,\ j = 0;$
**for** $n \in [1, N_{\text{tot}}]$ **do**
  $d_n^T = \text{norm}(\vec{C}_n - \vec{A}_0^{\text{T}})$ $d_n^R = \text{norm}(\vec{C}_n - \vec{A}_0^{\text{R}})$ **if** $d_n^T < d_{\text{lim}}$ **then**
    $\vec{C}_i^{\text{A}} = \vec{C}_n;\ i = i + 1$
  **end**
  **if** $d_n^R < d_{\text{lim}}$ **then**
    $\vec{C}_i^{Z} = \vec{C}_n;\ j = j + 1$
  **end**
**end**
$\mathbf{C}_{\text{tot}}^{\text{A}}=$ repmat($[\vec{C}_1^{\text{A}} \quad \vec{C}_2^{\text{A}} \quad \ldots \quad \vec{C}_i^{\text{A}}]$, 1, j)
$\mathbf{C}_{\text{tot}}^{\text{Z}}=$ repelem($[\vec{C}_1^{Z} \quad \vec{C}_2^{Z} \quad \ldots \quad \vec{C}_j^{Z}]$, 1, i)

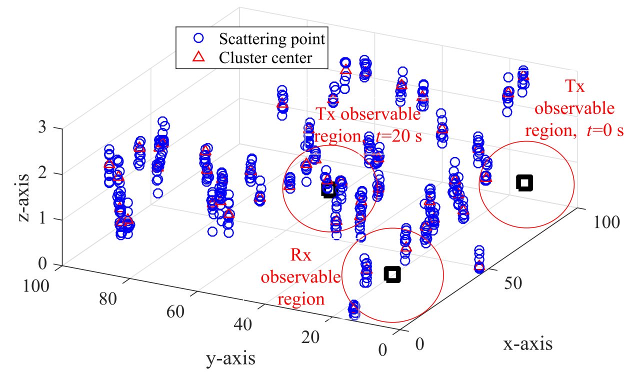


Fig. 4. Cluster generation using PPP in a pillar scenario ($|\vec{v}_T| = 3$ m/s, $|\vec{v}_R| = |\vec{v}_Z| = |\vec{v}_A| = 0$ m/s).

As for the time evolution in the pillar scenario, since scatterers in the far region will be sheltered by scatterers in the near region, only scatterers beside Tx and Rx should be considered in channel simulations. We set the scattering clusters observable regions at Tx and Rx, respectively. At each time interval, we first determine whether the cluster in the previous time interval is still in the Tx/Rx observable regions, remove the clusters that are not in the visible regions, and add the clusters that are newly generated in the visible regions to complete the birth/death evolution process. We assume that each scatterer in the Tx observable and in Rx observable regions can form a path. At each time instant $t$, the cluster sets of first bounce and last bounce can be obtained by Algorithm 1. It is worth mentioning that column vectors in $\mathbf{C}_{\text{tot}}^{\text{A}}$ and $\mathbf{C}_{\text{tot}}^{\text{Z}}$ represent the coordinates of first bounce and last bounce scatterers, that is, $\vec{C}_n^A = \mathbf{C}_{\text{tot}}^{\text{A}}(:, n)$ and $\vec{C}_n^Z = \mathbf{C}_{\text{tot}}^{\text{Z}}(:, n)$.

Fig. 4 illustrates the generation of scatterers in the pillar scenario. Red circles represent the observable region at the Tx side and Rx side. Note that with movement of Tx, the observable region of Tx is changing, causing the cluster birth/death phenomenon. Besides, for clarity, scenario-specific channel simulation parameters are listed in Table III. For the tunnel scenario, the angular spread parameters are set referring to the arched tunnel measurement results in [38] and cluster generation/recombination rates are chosen according to the conclusions mentioned in [39], that is, the higher-order MPCs have a faster decay rate in the far-field, resulting in the less cluster number in the far-field region. In terms of the pillar scenario, the scenario size is chosen as a medium size underground parking lot, and the scatterer intensity and radius of the cluster visible region are set according to [40]. Note that the radius of the cluster visible region is a parameter ranging from tens of meters to hundreds of meters and can be defined by users according to the propagation environment. Without the loss of generality, the value of visible region radius is set to 20 m in the simulation.

### *C. Channel Parameter Calculation*

After completing the generation of the scattering cluster parameters and the evolution of the birth/death process in each time interval, we use the Tx, Rx, and scatterers geometry relationship and the parameter generation method to generate corresponding cluster delay, power, and phase. For the antenna pair between the $p$th transmit antenna element and the $q$th

TABLE III
SCENARIO-SPECIFIC PARAMETERS

| Tunnel | $\lambda_G$ | $\lambda_R$ | AS($\phi_A^T/\phi_A^R$) | AS($\phi_E^T/\phi_E^R$) |
|---|---|---|---|---|
| Near-field | 20 | 1 | 0.41 | 0.18 |
| Far-field | 5 | 1 | 0.13 | 0.05 |
| Pillar | $\lambda_s$ | $d_{\lim}$ | Size of pillar scenario | |
| / | 0.005 | 20 m | 100 m×100 m×3 m | |

receive antenna element, the departure and arrival vectors of the $m$th ray in the $n$th cluster are expressed by

$$\vec{r}_{p,m_n}^{T} = \vec{C}_{m_n}^{A} - \vec{A}_{p}^{T} \tag{18}$$

$$\vec{r}_{q,m_n}^{R} = \vec{C}_{m_n}^{Z} - \vec{A}_{q}^{R} \tag{19}$$

where $\vec{A}_p^T$ and $\vec{A}_q^R$ denote the 3-D position vectors of the $p$th transmit antenna element and the $q$th receive antenna element, and can be written as

$$\vec{A}_p^T = \vec{A}_0^T + (p-1)\delta_T \begin{bmatrix} \cos\beta_A^T \cdot \cos\beta_E^T \\ \sin\beta_A^T \cdot \cos\beta_E^T \\ \sin\beta_E^T \end{bmatrix} \tag{20}$$

$$\vec{A}_q^R = \vec{A}_0^R + (q-1)\delta_R \begin{bmatrix} \cos\beta_A^R \cdot \cos\beta_E^R \\ \sin\beta_A^R \cdot \cos\beta_E^R \\ \sin\beta_E^R \end{bmatrix}. \tag{21}$$

Then the AAoA, AAoD, EAoA, and EAoD of the $m$th ray in the $n$th path can be obtained by

$$\phi_{A,m_n}^{T/R} = \arctan_2\left(r_{m_n,y}^{T/R}, r_{m_n,x}^{T/R}\right) \tag{22}$$

$$\phi_{E,m_n}^{T/R} = \arcsin\left(r_{m_n,z}^{T/R}, D_{m_n}^{T/R}\right) \tag{23}$$

where $r_{m_n,x}^{T/R}$, $r_{m_n,z}^{T/R}$, and $r_{m_n,z}^{T/R}$ stand for $x$, $y$, and $z$ coordinates of $\vec{r}_{m_n}^{T/R}$, and $D_{m_n}^{T/R}$ denotes the norm of $\vec{r}_{m_n}^{T/R}$. For clarity, the antenna element index subscripts $(p/q)$ are dropped.

Simultaneously, the AAoA, AAoD, EAoA, EAoD, and length of the LoS component can be calculated from the vector of the LoS component, which can be written as

$$\vec{r}_{pq}^{\text{LoS}} = \vec{A}_p^R - \vec{A}_q^T. \tag{24}$$

Similar to (22), (23), the AAoA, AAoD, EAoA, and EAoD of the LoS component can be calculated through inverse trigonometric function, and the propagation distance of the LoS component, $D_{pq}^{\text{LoS}}$, can be calculated as the norm of $\vec{r}_{pq}^{\text{LoS}}$. The delay and power of MPCs are determined by the propagation distance. For the $m$th ray in the $n$th path, the propagation delay can be expressed as

$$\tau_{pq,m_n}(t) = \left(D_{p,m_n}^T + D_{q,m_n}^R\right)/c + \tilde{\tau}_n \tag{25}$$

where $\tilde{\tau}_n$ is the time delay of virtual link between first and last bounces clusters, that is, $C_n^A$ and $C_n^Z$, and can be represented by $\tilde{\tau}_n = \tilde{d}_n/c + \tau_{\text{C,link}}$, in which $\tilde{d}_n$ denotes the distance between $C_n^A$ and $C_n^Z$, and $\tau_{\text{C,link}}$ is an exponentially distributed variable that can be generated by

$$\tau_{\text{C,link}} = -r_\tau \sigma_\tau \cdot \ln u_n \tag{26}$$

where $u_n$ is generated according to uniform distribution in (0, 1), $r_\tau$ denotes the delay scalar, and $\sigma_\tau$ denotes the delay spread [41]. Subsequently, the power of the $m$th ray in the $n$th path is determined by

$$P'_{pq,m_n}(t) = \left[\exp\left(-\tau_{pq,m_n}(t)\frac{r_\tau - 1}{r_\tau \sigma_\tau}\right)10^{-\frac{Y_n}{10}}\right] \tag{27}$$

where $Y_n$ is the per cluster shadowing term following a Gaussian distribution. The final ray powers are obtained by normalizing $P'_{pq,m_n}(t)$ as

$$P_{pq,m_n}(t) = P'_{pq,m_n}(t) / \sum_{n=1}^{N(t)} \sum_{m_n=1}^{M_n} P'_{pq,m_n}(t). \tag{28}$$

## III. Statistical Properties

### A. Time-Variant Delay PSD

The delay PSD $\Lambda_{pq}(t,\tau)$ intuitively reveal the power distribution the in time delay domain and is defined as

$$\Lambda_{pq}^{\tau}(t,\tau) = \sum_{n=1}^{N(t)} \sum_{m_n=1}^{M_n} P_{pq,m_n}(t)\delta\left(\tau - \tau_{m_n}(t)\right). \tag{29}$$

The temporal variation of delay PSD is caused by evolutions of clusters with respect to time. The variation trend of delay PSD will depend on the geometrical relationship updates of the underground scattering environment.

### B. Local STF-CF

To study the correlation characteristics, the local STF-CF between $h_{pq}(t,f)$ and $h_{\tilde{p}\tilde{q}}(t-\Delta t, f-\Delta f)$ is defined as

$$R_{pq,\tilde{p}\tilde{q}}(t,f;\Delta d,\Delta t,\Delta f) = \mathbb{E}\left\{h_{pq}(t,f)h_{\tilde{p}\tilde{q}}^{*}(t-\Delta t, f-\Delta f)\right\} \tag{30}$$

where $f$ and $\Delta f$ denote the baseband frequency and frequency difference, respectively. The spatial difference $\Delta d = \{\Delta d_T, \Delta d_R\}$ contains antenna element spacings at Tx and Rx, that is, $\Delta d_T = \delta_{\tilde{p}} - \delta_p$ and $\Delta d_R = \delta_{\tilde{q}} - \delta_q$. Substituting (3) into (30), the local STF-CF can be obtained by sum of the correlation of the LoS component and the correlation of the NLoS components as

$$\begin{aligned} R_{pq,\tilde{p}\tilde{q}}&(\Delta d,\Delta t,\Delta f;t,f) \\ &= \frac{K_R}{K_R+1} R_{pq,\tilde{p}\tilde{q}}^{\text{LoS}}(\Delta d,\Delta t,\Delta f;t,f) \\ &\quad + \frac{1}{K_R+1}\sum_{n=1}^{N(t)} R_{pq,\tilde{p}\tilde{q},n}^{\text{NLoS}}(\Delta d,\Delta t,\Delta f;t,f). \end{aligned} \tag{31}$$

The STF-CF of LoS component is calculated as

$$\begin{aligned} R_{pq,\tilde{p}\tilde{q}}^{\text{LoS}}&(\Delta d,\Delta t,\Delta f;t,f) \\ &= \left[P_{pq}^{\text{LoS}}(t) P_{\tilde{p}\tilde{q}}^{\text{LoS}}(t-\Delta t)\right]^{\frac{1}{2}} \\ &\quad \cdot e^{j\frac{2\pi(f_c-f)}{\lambda f_c}\left[D_{pq}^{\text{LoS}}(t) - D_{\tilde{p}\tilde{q}}^{\text{LoS}}(t-\Delta t)\right]} \cdot e^{j\frac{2\pi\Delta f}{\lambda f_c}\left[D_{\tilde{p}\tilde{q}}^{\text{LoS}}(t-\Delta t)\right]}. \end{aligned} \tag{32}$$

As for the local STF-CF of NLoS components, it can be calculated as

$$R^{\mathrm{NLoS}}_{pq,\tilde{p}\tilde{q},n}(\Delta d, \Delta t, \Delta f; t, f) = P_{\mathrm{s}}(t, \Delta t) \cdot \mathbb{E}\left\{ \sum_{m_n=1}^{M_n} a_{m_n} \cdot e^{j\frac{2\pi(f_c - f)}{\lambda f_c}\left[D_{pq,m_n}(t) - D_{\tilde{p}\tilde{q},m_n}(t-\Delta t)\right]} \cdot e^{j\frac{2\pi\Delta f}{\lambda f_c}\left[D_{\tilde{p}\tilde{q},m_n}(t-\Delta t)\right]} \right\} \tag{33}$$

where $a_{m_n}$ is the amplitude that can be expressed by $a_{m_n} = [P_{pq,m_n}(t)P_{\tilde{p}\tilde{q},m_n}(t-\Delta t)]^{\frac{1}{2}}$, and $P_{\mathrm{s}}(t, \Delta t)$ is the probability of the cluster surviving in period from $t - \Delta t$ to $t$.

### C. Doppler PSD

The movement of the Tx and Rx will bring shift in the carrier frequency, which is called Doppler frequency shift. Doppler PSD reflects the distribution of signal power at different Doppler frequencies, which can be obtained by the Fourier transform of the temporal autocorrelation function (ACF)

$$S_n(\nu, t) = \int_{-\infty}^{\infty} r_n(t, \Delta t) e^{-j2\pi\nu\Delta t} \mathrm{d}\Delta t \tag{34}$$

where $\nu$ is the Doppler frequency in Hz and $r_n(t, \Delta t)$ is the temporal ACF, which can be obtained by zeroing the Tx/Rx antenna spacing in the local STF-CF.

### D. Stationary Interval

The nonstationary property can be characterized by the stationary interval, which is defined as the maximum duration within which the channel can be seen as stationary. For mobile communication systems, the channel estimation frequency greatly depends on the value of the stationary interval.

Here, we introduce the method of local region of stationarity (LRS) to obtain the stationary interval [44]. First, the average power delay profile (PDP) is obtained by taking average of $N_{\mathrm{PDP}}$ PDPs as

$$\overline{P}_h(t_k, \tau) = \frac{1}{N_{\mathrm{PDP}}} \sum_{k}^{k+N_{\mathrm{PDP}}-1} \Lambda^{\tau}_{pq}(t_k, \tau). \tag{35}$$

The average time is chosen as $N_{\mathrm{PDP}} = 10$. The correlation coefficient between the average PDPs is defined as

$$c(t_k, \Delta t) = \frac{\int \overline{P_h}(t_k, \tau) \cdot \overline{P_h}(t_k + \Delta t, \tau) d\tau}{\max\left\{\int \overline{P_h}(t_k, \tau)^2 d\tau, \int \overline{P_h}(t_k + \Delta t, \tau)^2 d\tau\right\}}. \tag{36}$$

Next the stationary interval is obtained as the largest time duration within which the correlation coefficient beyond the certain threshold $c_{\mathrm{thresh}}$, that is,

$$T_s(t) = \max\left\{\Delta t \middle| c(t, \Delta t) \geq c_{\mathrm{thresh}}\right\}. \tag{37}$$

According to most current investigations, the correlation coefficient threshold is empirically set to 90% and certainly this value can be adjusted according to specific requirements [5].

### E. Angular Power Spectrum

The angular power spectrum reflects the distribution of channel power in angular domain. It can be acquired by power and angular parameters, and can be expressed as

$$\Lambda^R_{pq}\left(t, \phi^R_A, \phi^R_E\right) = \sum_{n=1}^{N(t)} \sum_{m_n=1}^{M_n} P_{pq,m_n}(t) \times \delta\left(\phi^R_A - \phi^R_{A,m_n}\right) \times \delta\left(\phi^R_E - \phi^E_{A,m_n}\right) \tag{38}$$

where $\phi^R_A$ and $\phi^R_E$ are AAoA and EAoA, respectively. Similarly, at the Tx side, the angular power spectrum can be obtained by the same method.

### F. LCR and AFD

The LCR and AFD describe how quickly the channel changes over time and are essential parameters in the design and evaluation of communication systems. The LCR is defined as the number of occurrences per unit time that the amplitude of the channel crosses a given threshold bottom-up (or top-down). The LCR of a channel model can be calculated by the following equation [45]:

$$N(r, t) = \frac{2r\sqrt{K_R + 1}}{\pi^{3/2}} \sqrt{\frac{b_2(t)}{b_0} - \frac{b_1^2(t)}{b_0^2}} e^{-K_R - (K_R+1)r^2} \times \int_0^{\pi/2} \cosh\left(2\sqrt{K_R(K_R+1)} r \cos\omega\right) \times \left[e^{-(\chi(t)\sin\omega)^2} + \sqrt{\pi}\chi(t)\sin\omega\,\mathrm{erf}(\chi(t)\sin\omega)\right] d\omega \tag{39}$$

where $\cosh(\cdot)$ refers to the hyperbolic cosine function and $\mathrm{erf}(\cdot)$ denotes the error function. Parameters $\chi(t)$ and $b_l(t)(l = 0, 1, 2)$ are written as

$$\chi(t) = \sqrt{\frac{K_R \cdot b_1(t)^2}{b_0 \cdot b_2(t) - b_1(t)^2}}. \tag{40}$$

According to the definition of temporal ACF, the $b_l(t)(l = 0, 1, 2)$ can be obtained as

$$b_l(t) = \frac{(2\pi)^l}{(K_R + 1)\lambda^l} \cdot \sum_{n=1}^{N(t)} \sum_{m_n=1}^{M_n} P_{pq,m_n}(t) \left(\vec{v}_T \cdot \vec{r}^{\,T}_{m_n} / \left|\vec{r}^{\,T}_{m_n}\right| + \vec{v}_R \cdot \vec{r}^{\,R}_{m_n} / \left|\vec{r}^{\,R}_{m_n}\right| - \vec{v}_A \cdot \vec{r}^{\,T}_{m_n} / \left|\vec{r}^{\,T}_{m_n}\right| - \vec{v}_Z \cdot \vec{r}^{\,R}_{m_n} / \left|\vec{r}^{\,R}_{m_n}\right|\right)^l. \tag{41}$$

The AFD is defined as the average time duration of the envelope amplitude under the certain threshold, which can be calculated according to LCR, that is,

$$L(r, t) = \frac{1 - \mathrm{Q}\left(\sqrt{2K_R}, \sqrt{2(K_R + 1)r^2}\right)}{N(r, t)} \tag{42}$$

where $\mathrm{Q}(\cdot)$ is the Marcum-Q function. Note that the calculation of the LCR and AFD in this article is based on the narrowband assumption, that is, the time delay difference between different clusters is not taken into account.

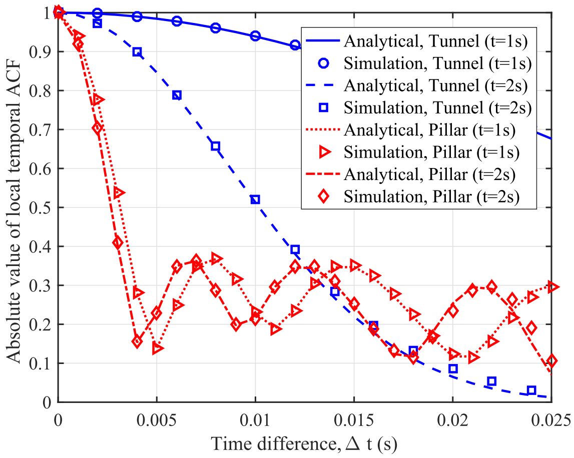


Fig. 5. Temporal ACFs at different scenarios and time instants ($\upsilon_T(t_0) = 10$ m/s, $a_T = 3$ m/s$^2$, $f_c = 2.5$ GHz, $\beta_{\mathrm{A}}^{T(R)} = \pi/3$, $\beta_E^{T(R)} = 0$).

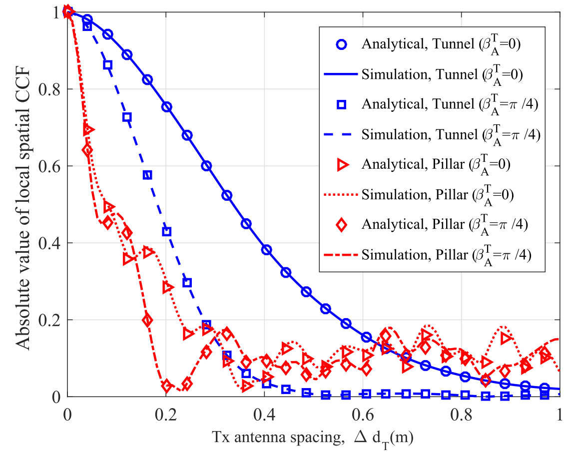


Fig. 6. Spatial CCFs at different scenarios and antenna array broadsides ($\upsilon_T(t_0) = 10$ m/s, $f_c = 2.5$ GHz, $\beta_{\mathrm{A}}^{R} = \pi/3$, and $\beta_E^{T(R)} = 0$).

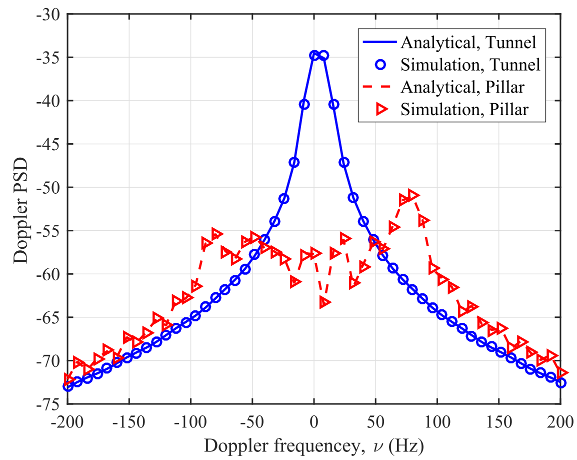


Fig. 7. Doppler PSD in different scenarios ($\upsilon_T(t_0) = 10$ m/s, $f_c = 2.5$ GHz, $\beta_{\mathrm{A}}^{T(R)} = \pi/3$ and, $\beta_E^{T(R)} = 0$).

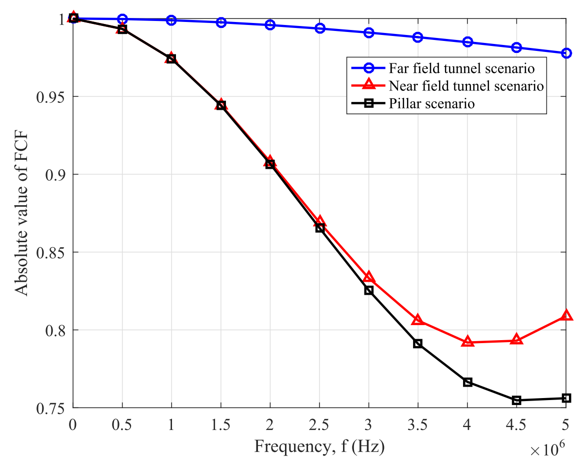


Fig. 8. FCFs in different scenarios ($f_c = 2.5$ GHz, $\beta_{\mathrm{A}}^{T(R)} = \pi/3$, $\beta_E^{T(R)} = 0$; pillar scenario and tunnel scenario near field: $\sigma_\tau = 10^{-7.5}$; tunnel scenario far-field: $\sigma_\tau = 10^{-8.5}$).

## IV. Results and Analysis

In this section, the simulation of statistical characteristics based on proposed channel model is provided. The channel simulation is realized on personal computer (Intel(R) Core(TM) i7-9700 CPU @3.0 GHz, 32.0 GB RAM) using MATLAB R2016. In the simulation, the observation time is [1s, 2s], the Tx and Rx are equipped with uniform linear arrays with the antenna spacing $\delta_T$ and $\delta_R$. Therefore, the distance from $A_1^T$ to $A_q^T$ and from $A_1^R$ to $A_q^R$ can be expressed as $(p-1)\delta_T$ and $(q-1)\delta_R$, respectively. The default parameters are set as follows: $f_c = 2.5$ GHz, $\tilde{p}(\tilde{q}) = 2$, $p(q) = 1$, $\beta_{\mathrm{A}}^{T(R)} = \pi/3$, and $\beta_E^{T(R)} = 0$. For the tunnel scenario, the generation and recombination rates are set to $\lambda_G = 20$, $\lambda_R = 1$ at near-field, and $\lambda_G = 5$ and $\lambda_R = 1$ at far-field. For the pillar scenario, the scatterer density is set to $0.002/\mathrm{m}^3$. The observable regions at Tx and Rx sides are spheres taking Tx and Rx as centers with 20 m radius. In addition, the simulation in this section are based on the horizontal propagation assumptions and the use of omnidirectional antennas at the Tx and Rx.

Fig. 5 shows the absolute value of the temporal ACF at different time instants for different scenarios. In the simulation, Rx is accelerated in a straight line with an initial velocity of 10 m/s and an acceleration of 3 m/s$^2$. It is found that the absolute value of the temporal ACF is larger in the tunnel scenario than in the pillar scenario. It may because the parameters of MPCs are similar in the tunnel scenario, while the parameters of MPCs are different in the pillar scenario. In addition, since the speed of Rx is set to the acceleration motion, the channel change rate gradually becomes larger so the temporal ACF gradually decreases. Finally, we compare the theoretical results and simulation results of different scenarios at different times, and the two fit well, reflecting the consistency of channel characteristic derivation and simulation.

Fig. 6 presents the absolute values of the spatial cross-correlation function (CCF) for different scenarios and antenna orientations. Since the MPCs come from similar directions in the tunnel scenario, the absolute value of the spatial CCF is larger in the tunnel scenario. This means that larger spatial complexing gain can be achieved in the pillar scenario. In addition, we can find that antenna orientation angle variation has a more significant effect on the spatial correlation in the tunnel scenario, while antenna orientation angle variation has a less significant effect on the spatial correlation in the pillar scenario.

Fig. 7 gives the Doppler PSD for different structure scenarios. It can be found that the Doppler PSD is more concentrated in the tunnel scenario, with larger power peaks

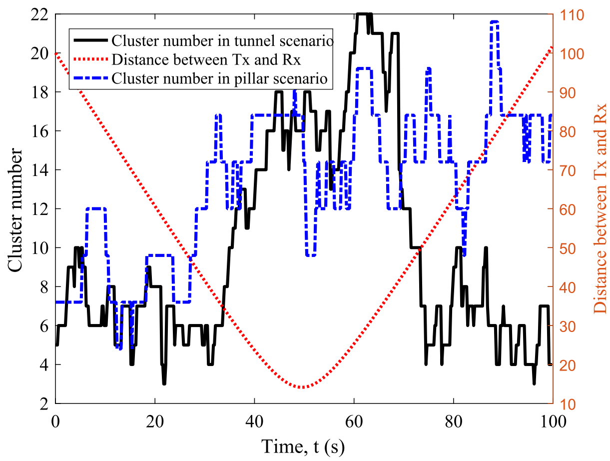


Fig. 9. Cluster number in different scenarios ($\upsilon_T(t_0) = 2$ m/s, $f_c = 2.5$ GHz, $\beta_{\mathrm{A}}^{T(R)} = \pi/3$, $\beta_E^{T(R)} = 0$).

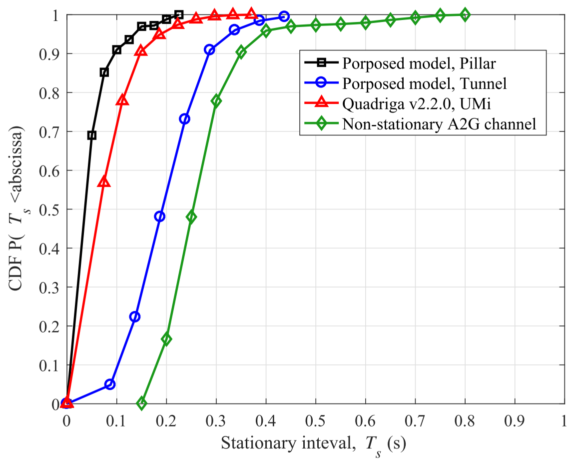


Fig. 10. Stationary intervals of different scenarios and different channel models ($\upsilon_T(t_0) = 4$ m/s, $f_c = 2.5$ GHz, $\beta_{\mathrm{A}}^{T(R)} = \pi/3$, $\beta_E^{T(R)} = 0$).

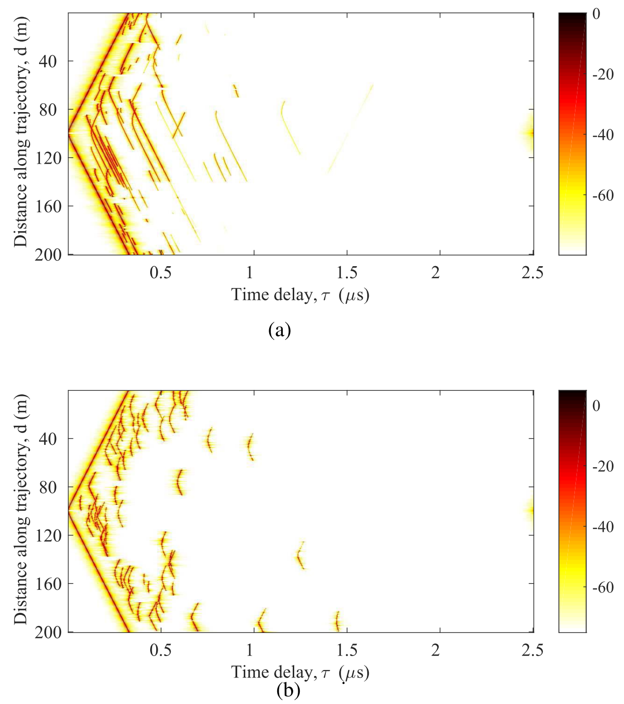


Fig. 11. Time-variant time-delay PSD of the proposed underground channel model ($\upsilon_T(t_0) = 10$ m/s, $f_c = 2.5$ GHz, $\beta_{\mathrm{A}}^{T(R)} = \pi/3$, and $\beta_E^{T(R)} = 0$). (a) Time-delay PSD in the tunnel scenario. (b) Time-delay PSD in the pillar scenario.

appearing, while the Doppler PSD is more dispersed in the pillar scenario, close to the U-shaped power spectrum in the isotropic channel scenario to a certain extent.

Fig. 8 presents the frequency correlation functions (FCFs) for pillar scenario and near/far fields in the tunnel scenario. The FCF represents the variation of the channel in the frequency domain. It can be observed that FCF descends slower in the far-field tunnel scenario, while FCFs in the pillar scenario and the near-field tunnel scenario have the similar variation trends. Usually coherent bandwidth is chosen as the bandwidth meeting the condition that FCF exceeds 90% threshold. Under the given parameter setting, the coherent bandwidths of the near-field tunnel channel and the pillar channel are about 2 MHz and that of the far-field tunnel channel is about 10 MHz, indicating more flat fading in the far-field tunnel channel.

Fig. 9 shows the path number in different structure scenarios. As the distance between Tx and Rx increases, due to the switching of channel parameters from near-field to far-field, the number of clusters in the tunnel scenario gradually decreases from 22 to 5, while for the pillar scenario, the number of clusters presents random fluctuation and distance between Tx and Rx has no significant effect on the number of clusters.

Fig. 10 gives the simulation results of stationary interval of different scenarios. It can be observed that the stationary intervals of the pillar scenario are smaller than those of the tunnel scenario, which illustrates that a higher channel estimation frequency should be used in the pillar scenario. Besides, we also provide the simulation results of existing channel models for comparison. Since that simple stochastic channel models such as traditional Rayleigh and Ricean models are based on the wide-sense-stationary assumption, they cannot characterize the time-variant environment and nonstationary propagation property. To quantify the nonstationary property in underground scenarios, we choose two nonstationary channel models, that is, quasi-deterministic radio channel generator (QuaDRiGa) [43] and nonstationary air-to-ground (A2G) channel model [31] for reference. The scenario of QuaDRiGa is set as overground urban micro (UMi) cell and scenario of nonstationary A2G channel model is set as an urban area with UAV height $h_U = 100$ m. With the same system configuration (carrier frequency, velocity, etc.) and stationary interval calculation method, it can be noticed that the stationary interval in the pillar scenario is shorter than stationary intervals of UMi and A2G scenarios. The reason is the dense distribution of scatterers in the pillar scenario. The distribution of the stationary interval in the tunnel scenario is between those of UMi and A2G scenarios because the A2G channel has more dominant LoS components. The analysis of nonstationary property can provide some references and guidance for the underground communication system design from the perspective of the propagation channel. For instance, the smaller stationary interval in the pillar scenario means that a higher channel estimation frequency should be considered in the system design.

Fig. 11 illustrates the delay PSD of different structure scenarios. The Rx trajectory is set to a linear track that comes close to Tx first and then moves away. In both the tunnel and pillar scenarios, it can be observed that the power of MPC

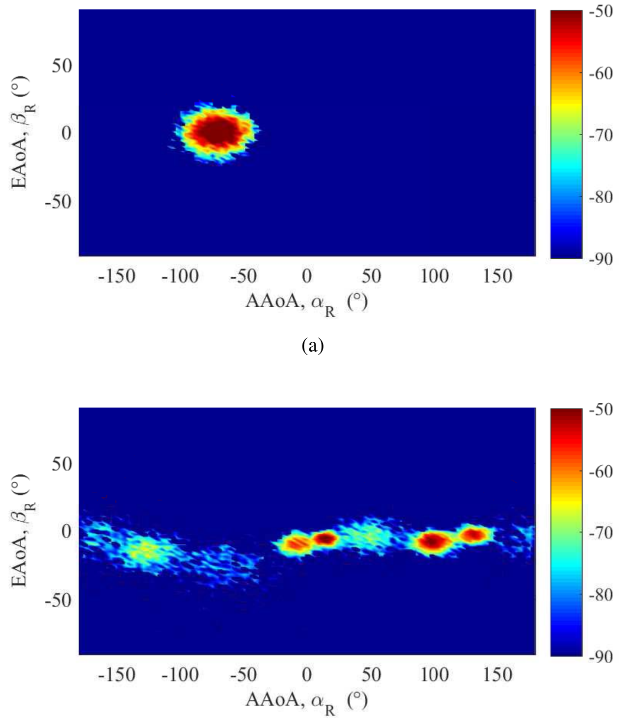


(a)

(b)

Fig. 12. Angular PSD of the proposed underground channel model ($\upsilon_T(t_0) = 10$ m/s, $f_c = 2.5$ GHz, $\beta_A^{T(R)} = \pi/3$, and $\beta_E^{T(R)} = 0$). (a) Angular PSD in the tunnel scenario. (b) Angular PSD in the pillar scenario.

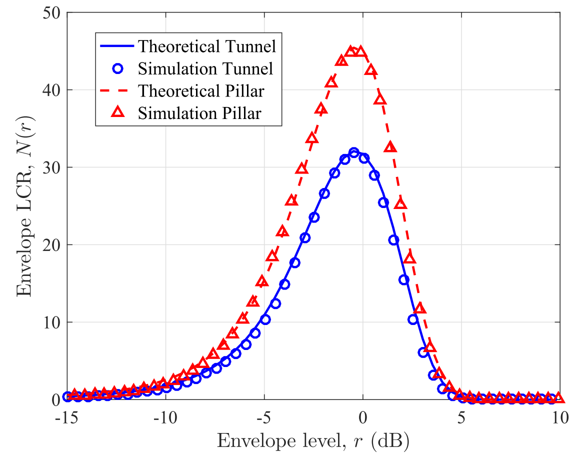


Fig. 13. LCR in different scenarios ($\upsilon_T(t_0) = 10$ m/s, $f_c = 2.5$ GHz, $\beta_A^{T(R)} = \pi/3$, and $\beta_E^{T(R)} = 0$).

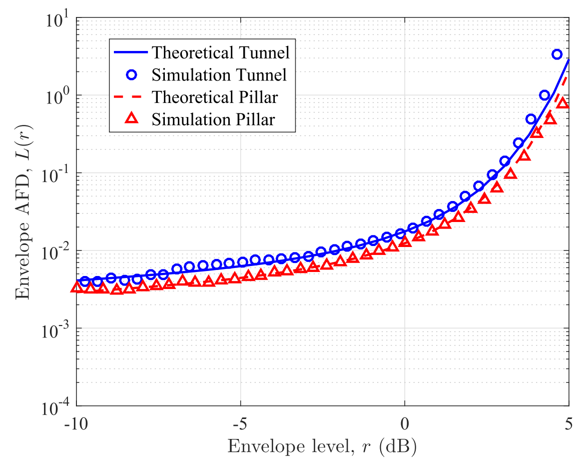


Fig. 14. AFD in different scenarios ($\upsilon_T(t_0) = 10$ m/s, $f_c = 2.5$ GHz, $\beta_A^{T(R)} = \pi/3$, and $\beta_E^{T(R)} = 0$).

gradually decreases and the delay of MPC gradually increases with the increasing distance between Tx and Rx. In the moving process, birth death of MPCs and drifting of powers and delays can be found both in the pillar and tunnel scenarios.

Fig. 12 shows angular PSDs at Rx for different structure scenarios. Without the loss of generality, we assume that both Tx and Rx are equipped with omnidirectional antennas. It can be observed that the multipath mostly coming from one direction with a higher concentration in the tunnel scenario. In the pillar scenario, the multipath comes from scattered clusters in different directions, with a large spread in the azimuth angle and a smaller spread in the elevation angle due to the top and bottom limitations.

Figs. 13 and 14 provide the simulation of LCR and AFD for different structure scenarios. Under the same Tx/Rx motion states, the tunnel structure scenario has the lower LCR and larger AFD, representing the slower channel time-varying. The pillar scenario has a higher LCR and smaller AFD, representing the faster channel time-varying.

## V. Channel Model Validation

### A. Channel Measurement Setup

To validate the proposed model, underground channel measurement is conducted based on our Keysight time-domain channel sounder in the underground garage of Shandong University, Qingdao Campus. The garage is about 120 m long, 40 m width, and 4 m height. The 3-D map of this garage and photograph taken during measurement are provided in Fig. 15. As shown in Fig. 16, the channel sounder Tx side consists of an M8190A arbitrary waveform generator (AWG) with a sampling rate of 12 GSa/s, an E8267D vector signal generator (VSG) with a frequency range of 100 kHz to 44 GHz, a high-precision HJ5418 GPS Rubidium clock, and a power amplifier (PA). The Rx side consists of an M9362A PXIe down converter, an M9352A PXI hybrid amplifier/attenuator, an M9300A PXIe frequency reference, an M9703B AXIe 12-bit digitizer, an E8257D analog signal generator, a GPS Rubidium clock, and a low noise amplifier (LNA). More detailed information of this sounder system is available in [46].

Due to the limitations of the available number of Tx/Rx antennas and PA/LNA, the channel measurement is conducted in the single-input single-output (SISO) mode. Omnidirectional discone antennas working in the range of 0.1–6 GHz with 2 dBi gain are utilized at both Tx and Rx sides. To enhance the effective measurement distance, a PA with 28 dB gain and an LNA with 35 dB gain are equipped at Tx and Rx sides, respectively. The measurements are conducted at 2.5 and 3.5 GHz bands with 625 MHz bandwidth. To enlarge the measurement system dynamic range, the pseudo-noise (PN) sequence with a length of $2^{12} = 4096$ is utilized as the baseband measurement waveform, and a processing gain of $G_{\mathrm{wa}} = 10\log_{10}2^{12} = 36$ dB is realized. Considering the standard thermal noise power density as $-174$ dBm/Hz, the receiving noise power is $P_n = -174$ dBm/Hz $+ 88$ dBHz $+ 35$ dB $= -51$ dBm. Taking

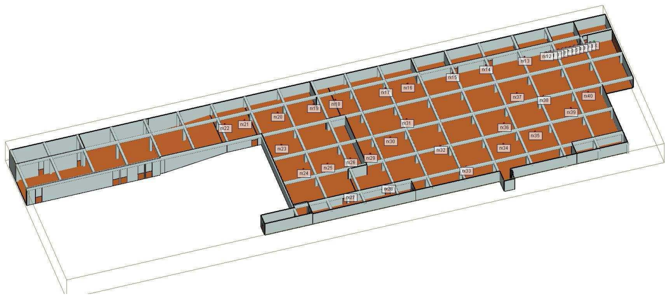

(a)

(b)

(c)

Fig. 15. Underground channel measurement scenario. (a) 3-D map of measurement garage. (b) Measurement process (Rx side). (c) Measurement process (Tx side).

$P_m = 5$ dB as margin, the dynamic range can be obtained as

$$D_r = P_t + G_{\text{PA}} + G_t + G_r + G_{\text{LNA}} + G_{\text{wa}} - P_n - P_m - L_{\text{sys}} = 146 \text{ dB} \quad (43)$$

where $G_t$ and $G_r$ are the gains of Tx and Rx antenna, respectively, $G_{\text{PA}}$ is the gain of the PA, $P_t = 0$ dBm is the power of the transmitting signal, $G_{\text{LNA}}$ is the gain of LNA, and $L_{\text{sys}} = 10$ dB is the attenuation caused by the measurement system (including attenuations of cable, adapter, etc.). This value of dynamic range means that measurement system can identify the MPC with maximum attenuation as 146 dB.

Besides, 404 and 500 zero points are added at the start and end of the waveform, respectively, to leave the time for amplifier response of power ramp up/down. To mitigate the inter symbol interference (ISI), the transmitted waveform is interpolated with two times and filtered by a root raised cosine (RRC) pulse shaping filter with a roll-off factor of 0.35. The received signal is also filtered by the same matched filter and down-sampled with two times.

In the measurement, the Rx is fixed at the entrance of garage, and Tx is slowly moving in the garage. At both 2.5 and 3.5 GHz bands, we measure 40 points in the garage. The scenario layout and the coordinates of these points are marked in Fig. 15(a).

### *B. Measurement Data Processing*

To eliminate the frequency response brought by the sounder, we first use back-to-back calibration signal to calibrate the measurement system [46], and obtain the attenuation and time delay of the signal caused by the measurement system. Then the relative CIRs at each measurement points can be calculated by

$$h(\tau) = \text{IFFT}(H(f)) = \text{IFFT}(Y_{\text{rx}}(f)/X_{\text{tx}}(f)) \quad (44)$$

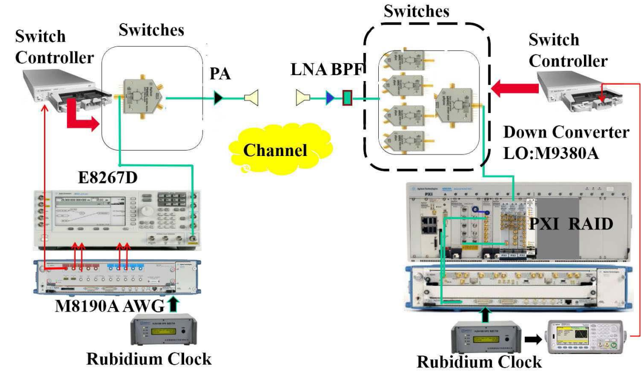


Fig. 16. Keysight time-domain channel sounder.

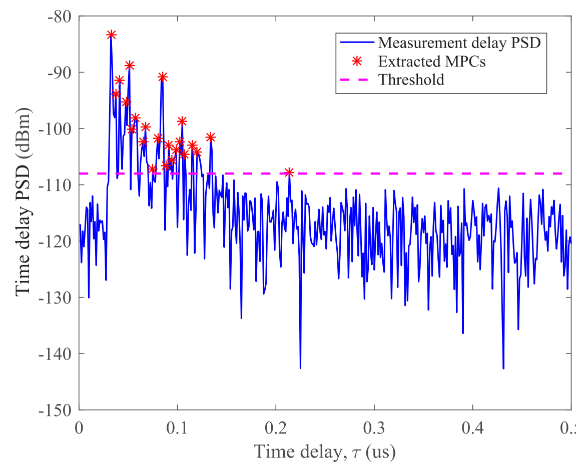


Fig. 17. Measurement continues delay PSD and extracted MPCs at point 38.

where $X_{\text{tx}}(f)$ and $Y_{\text{rx}}(f)$ are frequency-domain responses of transmitting and receiving signals, respectively.

The MPCs can be extracted by the peak search algorithm in continuous delay PSD, that is, $|h(\tau)|^2$. The complex amplitude, power, and time delay of the $l$th MPC are denoted by $h_l$, $P_l$, and $\tau_l$, respectively. The peak searching power threshold is chosen as maximum value between maximum power minus 20 dB and average noise floor plus 5 dB [46]. The MPCs extracting result at point 38 is presented in Fig. 17. The received power $P_r$ is calculated by summing all powers of MPCs. To characterize the large-scale fading, the path loss is given by

$$PL(\text{dB}) = -P_r + G_t + G_r + G_{\text{PA}} + P_t + G_{\text{LNA}} - L_{\text{sys}}. \quad (45)$$

To keep consistency between channel measurement and model simulation in small-scale fading characteristic analysis, the measurement MPC powers at each measurement point are normalized same as (28) and normalized received signal envelope can be obtained by

$$a = \sum_{l=1}^{L} h_l e^{2\pi f \tau_l} \cdot \left( \sum_{l=1}^{L} P_l \right)^{-1/2}. \quad (46)$$

To characterize the time delay properties, the root mean square (rms) delay spread can be expressed by

$$\sigma_\tau = \sqrt{\frac{\sum_{l=1}^{L} P_l \tau_l^2}{\sum_{l=1}^{L} P_l} - \left( \frac{\sum_{l=1}^{L} P_l \tau_l}{\sum_{l=1}^{L} P_l} \right)^2}. \quad (47)$$

TABLE IV
FREQUENCY-SPECIFIC FITTING PARAMETERS

| Parameters | A | $n$ | $K_R$(dB) | $\sigma_\tau$(dB) | $r_\tau$ | $\sigma_n$ |
|---|---|---|---|---|---|---|
| 2.5 GHz | -39.32 | 1.96 | 12.0 | -7.31 | 2 | 2.5 |
| 3.5 GHz | -39.27 | 2.19 | 10.2 | -7.53 | 2 | 2.5 |

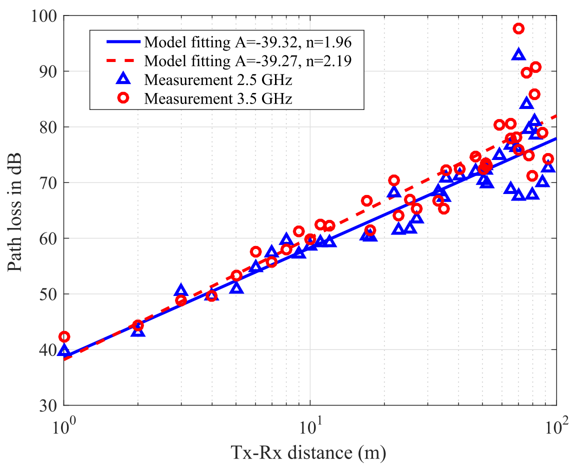


Fig. 18. Measurement path loss and fitting results at 2.5 and 3.5 GHz.

### C. Comparison With Measurement Data

To ensure the accuracy and usefulness of the proposed channel model, we use the channel measurement data to validate the proposed channel model. The simulation parameter set is estimated based on the minimum mean square error (MMSE) criterion, that is, $\varepsilon = |\hat{F} - F(\mathcal{P})|^2$, in which $\hat{F}$ is the measurement statistical property such as CDF of the amplitude, $F$ is the derived statistical property, and $\mathcal{P}$ is the estimated parameter set. Note that only a small number of parameters have significant influence on the targeted statistical property, so estimated parameter set $\mathcal{P}$ only includes a part of simulation parameters.

The path loss measurement results and model fitting results are shown in Fig. 18. Since the garage size limitation, the measurement distance is in the range of 1–100 m. It can be observed that path losses increase linearly with log distance between Tx and Rx at 2.5/3.5 GHz bands. Due to the limitation of measurement distance, the break point is not found in our measurement result. Substituting cross section width $w = 40$ m and height $h = 4$ m in (2), the break point distances can be calculated as 16 km at 3.5 GHz and 13 km at 2.5 GHz, which are greater than the maximum measurement distance. Therefore, the single slope path loss model is used in fitting. The 3.5 GHz band has the larger path loss exponent compared to 2.5 GHz band. It is worth mentioning that path loss exponent at 2.5 GHz ($n = 1.96$) is a little bit smaller than that of free space path loss ($n = 2$). Though a lot of obstacles exist in the pillar scenario, the path loss exponent in the measurement pillar scenario is still close to the free space path loss exponent. The reason behind may be the ceiling and floor forming a nonobvious waveguide structure.

For the small-scale fading, the measurement results of normalized signal amplitudes are provided in Fig. 19. It can be found that the CDFs of amplitudes at 2.5 and 3.5 GHz are similar, and the amplitudes at 2.5 GHz show slightly more dispersion. The fitting parameters including Ricean K factor

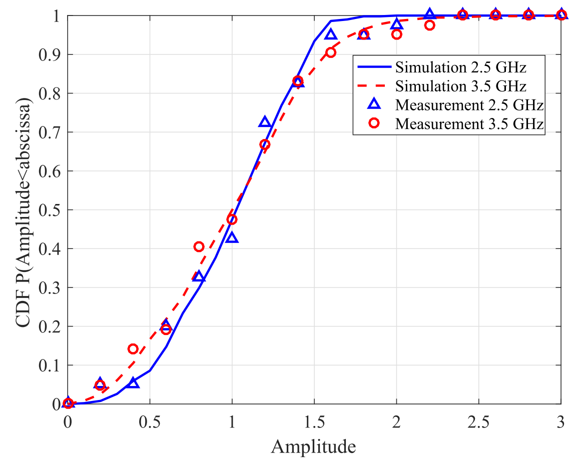


Fig. 19. Normalized measurement amplitudes and fitting results at 2.5 and 3.5 GHz.

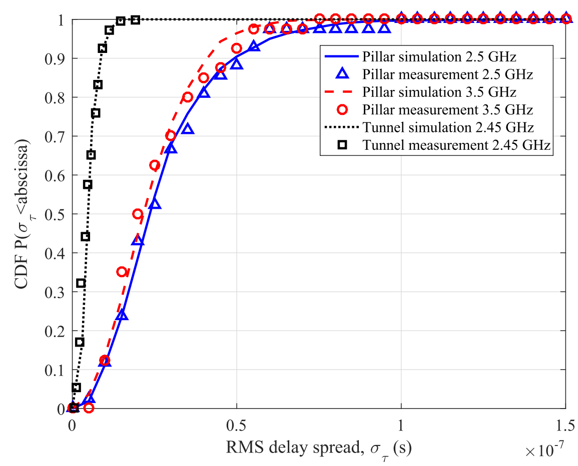


Fig. 20. Measurement rms delay spread and fitting results at 2.5 (2.45 GHz in the tunnel for reference [49]) and 3.5 GHz.

TABLE V
K–S TEST D VALUES FOR DIFFERENT STATISTICAL PROPERTIES

| Statistical properties | Amplitude | RMS delay spread | 95% significance upper quantile |
|---|---|---|---|
| 2.5 GHz | 0.04 | 0.06 | 0.21 [50] |
| 3.5 GHz | 0.07 | 0.08 | |

$K_R$ and dispersion of cluster $\sigma_n$ are provided in Table IV. For the time delay properties, the measurement rms delay spreads are shown in Fig. 20. The difference of delay spread between 2.5 and 3.5 GHz is less marked. Besides, the fitting parameters including the expectation of delay spread and per cluster spread are provided in Table IV. For comparison, the measurement rms delay spread at the tunnel scenario and the fitting results are also provided. Since there is no available tunnel measurement result at 2.5 or 3.5 GHz, the tunnel measurement result at adjacent frequency band 2.45 GHz is chosen for reference. The results are obtained in mine shaft by wideband-frequency domain measurement and detailed measurement set is available in [49]. From the comparison, it can be observed that at similar frequency bands, the rms delay spread at the tunnel scenario is much smaller than that of pillar scenario.

To further validate the accuracy of the proposed channel model, we implement the Kolmogorov–Smirnov (K–S) test to give an accuracy measure. The K–S test is widely used as a nonparametric test of equality for 1-D probability distributions. The K–S distance values (D values) between simulation results and measurement results for different statistical properties and frequencies are provided in Table V. Through the comparison, we can see that D values of the proposed model are far below the upper quantile of 95% significant level, indicating the accuracy and reliability of the proposed channel model.

## VI. Conclusion

In this article, a general 3-D nonstationary model for underground vehicular channels has been proposed based on different underground space structure scenarios. Different cluster generation and evolution mechanisms for the pillar and tunnel scenarios have been introduced into the proposed model. Based on the proposed channel model, we have derived the statistical properties of different underground scenarios, including temporal ACF, spatial CCF, Doppler PSD, LCR, and AFD. The theoretical derivation results fit well with the simulation results, which verifies the correctness of both theoretical derivations and simulations. Based on the derived and simulated results, we have found that under the same Tx/Rx trajectory and antenna configuration, the channel is more stable and changes slower w.r.t. time in the tunnel scenario, while in the pillar scenario, the spatial correlation is usually smaller, that is, the larger spatial diversity gain can be achieved. In addition, underground channel measurements have been conducted to investigate channel characteristics at different frequency bands (2.5/3.5 GHz). Measurement and simulation results have been compared to verify the accuracy and practicality of our proposed model.

## References

[1] A. Hrovat, G. Kandus, and T. Javornik, "A survey of radio propagation modeling for tunnels," *IEEE Commun. Surveys Tuts.*, vol. 16, no. 2, pp. 658–669, 2nd Quart., 2014.

[2] S. Yarkan, S. Guzelgoz, H. Arslan, and R. R. Murphy, "Underground mine communications: A survey," *IEEE Commun. Surveys Tuts.*, vol. 11, no. 3, pp. 125–142, 3rd Quart., 2009.

[3] C. X. Wang, J. Huang, H. Wang, X. Gao, X. You, and Y. Hao, "6G wireless channel measurements and models: Trends and challenges," *IEEE Veh. Technol. Mag.*, vol. 15, no. 4, pp. 22–32, Dec. 2020.

[4] X.-H. You et al., "Towards 6G wireless communication networks: Vision, enabling technologies, and new paradigm shifts," *Sci. China Inf. Sci.*, vol. 64, no. 1, pp. 1–74, Jan. 2021, doi: 10.1007/s11432-020-2955-6.

[5] C.-X. Wang, J. Bian, J. Sun, W. Zhang, and M. Zhang, "A survey of 5G channel measurements and models," *IEEE Commun. Surveys Tuts.*, vol. 20, no. 4, pp. 3142–3168, 4th Quart., 2018.

[6] Y. Liu, C.-X. Wang, C. F. Lopez, G. Goussetis, Y. Yang, and G. K. Karagiannidis, "3D non-stationary wideband tunnel channel models for 5G high-speed train wireless communications," *IEEE Trans. Intell. Transp. Syst.*, vol. 21, no. 1, pp. 259–272, Jan. 2020.

[7] C. X. Wang, A. Ghazal, B. Ai, P. Fan, and Y. Liu, "Channel measurements and models for high-speed train communication systems: A survey," *IEEE Commun. Surveys Tuts.*, vol. 18, no. 2, pp. 974–987, 2nd Quart., 2015.

[8] H. C. Nguyen, L. C. Gimenez, I. Z. Kovacs, I. Rodriguez, T. B. Sorensen, and P. Mogensen, "A simple statistical signal loss model for deep underground garage," in *Proc. IEEE 84th Veh. Technol. Conf. (VTC-Fall)*, Sep. 2016, pp. 1–5.

[9] R. Sun, D. W. Matolak, and P. Liu, "5-GHz V2V channel characteristics for parking garages," *IEEE Trans. Veh. Technol.*, vol. 66, no. 5, pp. 3538–3547, May 2017.

[10] J.-Y. Lee et al., "UWB propagation measurements in vehicular environments," in *Proc. IEEE Radio Wireless Symp.*, Jan. 2009, pp. 236–239.

[11] J.-Y. Lee, "UWB channel modeling in roadway and indoor parking environments," *IEEE Trans. Veh. Technol.*, vol. 59, no. 7, pp. 3171–3180, Sep. 2010.

[12] M. Yang et al., "V2V channel characterization and modeling for underground parking garages," *China Commun.*, vol. 16, no. 9, pp. 93–105, Sep. 2019.

[13] M. Lienard, P. Degauque, and P. Laly, "Communication and distance measurement in subway tunnels using natural propagation," in *Proc. 5th IEEE Int. Caracas Conf. Devices, Circuits Syst.*, Nov. 2004, pp. 240–243.

[14] M. Lienard, P. Degauque, J. Baudet, and D. Degardin, "Investigation on MIMO channels in subway tunnels," *IEEE J. Sel. Areas Commun.*, vol. 21, no. 3, pp. 332–339, Apr. 2003.

[15] J. A. Valdesueiro, B. Izquierdo, and J. Romeu, "MIMO channel measurement campaign in subway tunnels," in *Proc. EuCAP*, Barcelona, Spain, Apr. 2010, pp. 1–4.

[16] X. Zhang, N. Sood, and C. D. Sarris, "Fast radio-wave propagation modeling in tunnels with a hybrid vector parabolic equation/waveguide mode theory method," *IEEE Trans. Antennas Propag.*, vol. 66, no. 12, pp. 6540–6551, Dec. 2018.

[17] K. Guan, Z. Zhong, J. I. Alonso, and C. Briso-Rodriguez, "Measurement of distributed antenna systems at 2.4 GHz in a realistic subway tunnel environment," *IEEE Trans. Veh. Technol.*, vol. 61, no. 2, pp. 834–837, Feb. 2012.

[18] J. A. Valdesueiro, B. Izquierdo, and J. Romeu, "MIMO channel measurement campaign in subway tunnels," in *Proc. EuCAP*, Barcelona, Spain, Apr. 2010, pp. 1–4.

[19] C. Briso-Rodriguez, P. Fratilescu, and Y. Xu, "Path loss modeling for train-to-train communications in subway tunnels at 900/2400 MHz," *IEEE Antennas Wireless Propag. Lett.*, vol. 18, no. 6, pp. 1164–1168, Jun. 2019.

[20] C. Briso-Rodriguez, J. M. Cruz, and J. I. Alonso, "Measurements and modeling of distributed antenna systems in railway tunnels," *IEEE Trans. Veh. Technol.*, vol. 56, no. 5, pp. 2870–2879, Sep. 2007.

[21] J.-M. Molina-Garcia-Pardo, M. Lienard, A. Nasr, and P. Degauque, "Wideband analysis of large scale and small scale fading in tunnels," in *Proc. 8th Int. Conf. ITS Telecommun.*, Oct. 2008, pp. 270–273.

[22] H. Qiu et al., "Emulation of radio technologies for railways: A tapped-delay-line channel model for tunnels," *IEEE Access*, vol. 9, pp. 1512–1523, 2021.

[23] A. Chehri, P. Fortier, and P.-M. Tardif, "CTHp1–8: Measurements and modeling of line-of-sight UWB channel in underground mines," in *Proc. IEEE Globecom*, Nov. 2006, pp. 1–5.

[24] A. Chehri, P. Fortier, and P.-M. Tardif, "Frequency domain analysis of UWB channel propagation in underground mines," in *Proc. IEEE Veh. Technol. Conf.*, Sep. 2006, pp. 1–5.

[25] A. Chehri, P. Fortier, H. Aniss, and P.-M. Tardif, "UWB spatial fading and small scale characterization in underground mines," in *Proc. 23rd Biennial Symp. Commun.*, Jun. 2006, pp. 213–218.

[26] Z. Sun and I. F. Akyildiz, "Channel modeling and analysis for wireless networks in underground mines and road tunnels," *IEEE Trans. Commun.*, vol. 58, no. 6, pp. 1758–1768, Jun. 2010.

[27] M. Lienard and P. Degauque, "Natural wave propagation in mine environments," *IEEE Trans. Antennas Propag.*, vol. 48, no. 9, pp. 1326–1339, Sep. 2000.

[28] A. Ranjan, H. B. Sahu, and P. Misra, "Wave propagation model for wireless communication in underground mines," in *Proc. IEEE Bombay Sect. Symp. (IBSS)*, Sep. 2015, pp. 1–5.

[29] A. E. Forooshani, S. Bashir, D. G. Michelson, and S. Noghanian, "A survey of wireless communications and propagation modeling in underground mines," *IEEE Commun. Surveys Tuts.*, vol. 15, no. 4, pp. 1524–1545, 4th Quart., 2013.

[30] C.-X. Wang, Z. Lv, X. Gao, X. You, Y. Hao, and H. Haas, "Pervasive wireless channel modeling theory and applications to 6G GBSMs for all frequency bands and all scenarios," *IEEE Trans. Veh. Technol.*, vol. 71, no. 9, pp. 9159–9173, Sep. 2022.

[31] H. Chang et al., "A novel nonstationary 6G UAV-to-ground wireless channel model with 3-D arbitrary trajectory changes," *IEEE Internet Things J.*, vol. 8, no. 12, pp. 9865–9877, Jun. 2021.

[32] Q. Zhu et al., "A novel 3D non-stationary wireless MIMO channel simulator and hardware emulator," *IEEE Trans. Commun.*, vol. 66, no. 9, pp. 3865–3878, Sep. 2018.

[33] Z. Ma, B. Ai, R. He, Z. Zhong, and M. Yang, "A non-stationary geometry-based MIMO channel model for millimeter-wave UAV networks," *IEEE J. Sel. Areas Commun.*, vol. 39, no. 10, pp. 2960–2974, Oct. 2021.

[34] Z. Ma et al., "Modeling and analysis of MIMO multipath channels with aerial intelligent reflecting surface," *IEEE J. Sel. Areas Commun.*, vol. 40, no. 10, pp. 3027–3040, Oct. 2022.

[35] L. Bai, Z. Huang, X. Zhang, and X. Cheng, "A non-stationary 3D model for 6G massive MIMO mmWave UAV channels," *IEEE Trans. Wireless Commun.*, vol. 21, no. 6, pp. 4325–4339, Jun. 2022.

[36] Q. Zhu, X. Dang, D. Xu, and X. Chen, "Highly efficient rejection method for generating Nakagami-m sequences," *Electron. Lett.*, vol. 47, no. 19, pp. 1100–1101, 2011.

[37] S. Wu, C.-X. Wang, E.-H.-M. Aggoune, M. M. Alwakeel, and X. You, "A general 3-D non-stationary 5G wireless channel model," *IEEE Trans. Commun.*, vol. 66, no. 7, pp. 3065–3078, Jul. 2018.

[38] C. Garcia-Pardo, J.-M. Molina-Garcia-Pardo, M. Lienard, D. P. Gaillot, and P. Degauque, "Double directional channel measurements in an arched tunnel and interpretation using ray tracing in a rectangular tunnel," *Prog. Electromagn. Res. M*, vol. 22, pp. 91–107, 2012.

[39] A. E. Forooshani, S. Noghanian, and D. G. Michelson, "Characterization of angular spread in underground tunnels based on the multimode waveguide model," *IEEE Trans. Commun.*, vol. 62, no. 11, pp. 4126–4133, Nov. 2014.

[40] J. Flordelis, X. Li, O. Edfors, and F. Tufvesson, "Massive MIMO extensions to the COST 2100 channel model: Modeling and validation," *IEEE Trans. Wireless Commun.*, vol. 19, no. 1, pp. 380–394, Jan. 2020.

[41] J. Bian, C.-X. Wang, X. Q. Gao, X. You, and M. Zhang, "A general 3D non-stationary wireless channel model for 5G and beyond," *IEEE Trans. Wireless Commun.*, vol. 20, no. 5, pp. 3211–3224, May 2021.

[42] T. Klemenschits and E. Bonek, "Radio coverage of road tunnels at 900 and 1800 MHz by discrete antennas," in *Proc. 5th IEEE Int. Symp. Pers., Indoor Mobile Radio Commun., Wireless Netw. Catching Mobile Future.*, Sep. 1994, pp. 411–415.

[43] S. Jaeckel, L. Raschkowski, L. Thiele, F. Burkhardt, and E. Everlein, *QuaDRiGa-Quasi Deterministic Radio Channel Generator, User Manual and Documentation*, Berlin, Germany: Fraunhofer Hernrich Hertz Institute, v2.2.0, 2019.

[44] B. Chen, Z. Zhong, and B. Ai, "Stationarity intervals of time-variant channel in high speed railway scenario," *China Commun.*, vol. 9, no. 8, pp. 64–70, Aug. 2012.

[45] J. Bian et al., "A winner+ based 3D non-stationary wideband MIMO channel model," *IEEE Trans. Wireless Commun.*, vol. 17, no. 3, pp. 1755–1767, Mar. 2018.

[46] J. Huang, C.-X. Wang, H. Chang, J. Sun, and X. Q. Gao, "Multi-frequency multi-scenario millimeter wave MIMO channel measurements and modeling for B5G wireless communication systems," *IEEE J. Sel. Areas Commun.*, vol. 38, no. 9, pp. 2010–2025, Sep. 2020.

[47] *Study on Channel Model for Frequencies From 0.5 to 100 GHz*, Standard 3GPP TR 38.901 v14.1.0, Tech. Rep., 2017.

[48] S. M. Ross, *Simulation*. New York, NY, USA: Academic Press, 2008.

[49] S. Xue and J. Tan, "Radio channel characterizations at 2.4 GHz in mine shaft environment," in *Proc. WPMC*, 2017, pp. 138–142.

[50] L. H. Miller, "Tables of percentage points of Kolmogorov statistics," *J. Amer. Stat. Assoc.*, vol. 51, pp. 111–121, Mar. 1956.


**Hengtai Chang** (Member, IEEE) received the B.Sc. and Ph.D. degrees from the School of Information Science and Engineering, Shandong University, Jinan, China, in 2016 and 2021, respectively.

He is currently a Post-Doctoral Research Associate at the Purple Mountain Laboratories, Nanjing, China, and a Post-Doctoral Research Associate at the China National Mobile Communications Research Laboratory, Southeast University, Nanjing. His current research interests include unmanned aerial vehicle (UAV) communications, wireless propagation channel measurements and channel modeling, and B5G/6G wireless communications.

**Cheng-Xiang Wang** (Fellow, IEEE) received the B.Sc. and M.Eng. degrees in communication and information systems from Shandong University, Jinan, China, in 1997 and 2000, respectively, and the Ph.D. degree in wireless communications from Aalborg University, Aalborg, Denmark, in 2004.

He was a Research Assistant with the Hamburg University of Technology, Hamburg, Germany, from 2000 to 2001, a Visiting Researcher with Siemens AG Mobile Phones, Munich, Germany, in 2004, and a Research Fellow with the University of Agder, Grimstad, Norway, from 2001 to 2005. Since 2005, he has been with Heriot-Watt University, Edinburgh, U.K., where he was promoted to a Professor in 2011. In 2018, he joined as a Professor with Southeast University, Nanjing, China. He is also a part-time Professor with the Purple Mountain Laboratories, Nanjing. He has authored four books, three book chapters, and more than 480 papers in refereed journals and conference proceedings, including 27 highly cited articles. He has also delivered 24 invited keynote speeches/talks and 14 tutorials in international conferences. His current research interests include wireless channel measurements and modeling, 6G wireless communication networks, and electromagnetic information theory.

Dr. Wang is a member of the Academia Europaea (the Academy of Europe) and the European Academy of Sciences and Arts (EASA), a fellow of the Royal Society of Edinburgh (FRSE), the Institution of Engineering and Technology (IET), the China Institute of Communications (CIC), the IEEE Communications Society Distinguished Lecturer in 2019 and 2020, and a Highly-Cited Researcher recognized by Clarivate Analytics from 2017 to 2020, and one of the most cited Chinese Researchers recognized by Elsevier in 2021. He is currently an Executive Editorial Committee Member of the IEEE TRANSACTIONS ON WIRELESS COMMUNICATIONS. He has served as a TPC member, a TPC chair, and a general chair for more than 80 international conferences. He received 15 Best Paper Awards from IEEE Global Communications Conference (GLOBECOM) in 2010, IEEE International Conference on Communication Technology (ICCT) in 2011, International Conference on Intelligent Transportation Systems Telecommunications (ITST) in 2012, IEEE Vehicular Technology Conference (VTC) in Spring 2013, International Wireless Communications and Mobile Computing Conference (IWCMC) in 2015, IWCMC in 2016, IEEE/CIC International Conference on Communications in China (ICCC) in 2016, International Symposium on Wireless Personal Multimedia Communications (WPMC) in 2016, Wireless and Optical Communications Conference (WOCC) in 2019, IWCMC in 2020, International Conference on Wireless Communications and Signal Processing (WCSP) in 2020, International Conference on Communications Signal Processing and Systems (CSPS) in 2021, WCSP in 2021, and IEEE/CIC ICCC in 2022. Also, he received the AI 2000 Most Influential Scholar Award Honorable Mention from 2020 to 2022 for recognition of his outstanding and vibrant contributions in the field of the Internet of Things. He has served as an Editor for over ten international journals, including the IEEE TRANSACTIONS ON WIRELESS COMMUNICATIONS from 2007 to 2009, the IEEE TRANSACTIONS ON VEHICULAR TECHNOLOGY from 2011 to 2017, and the IEEE TRANSACTIONS ON COMMUNICATIONS from 2015 to 2017. He was the Guest Editor of the IEEE JOURNAL ON SELECTED AREAS IN COMMUNICATIONS. He was the Lead Guest Editor of the *Special Issue on Vehicular Communications and Networks*, *Special Issue on Spectrum and Energy Efficient Design of Wireless Communication Networks*, and *Special Issue on Airborne Communication Networks*. He was also the Guest Editor for the SPECIAL ISSUE ON WIRELESS BIG DATA OF THE IEEE TRANSACTIONS ON BIG DATA. He is the Guest Editor for the SPECIAL ISSUE ON INTELLIGENT RESOURCE MANAGEMENT FOR 5G AND BEYOND OF THE IEEE TRANSACTIONS ON COGNITIVE COMMUNICATIONS AND NETWORKING.

**Yu Liu** (Member, IEEE) received the Ph.D. degree in communication and information systems from Shandong University, Jinan, China, in 2017.

From 2015 to 2017, she was a Visiting Scholar with the School of Engineering and Physical Sciences, Heriot-Watt University, Edinburgh, U.K. From 2017 to 2019, she was a Post-Doctoral Research Associate with the School of Information Science and Engineering, Shandong University. Since 2019, she has been an Associate Professor with the School of Microelectronics, Shandong University. Her main research interests include nonstationary wireless multiple-input multiple-output (MIMO) channel modeling, high-speed train wireless propagation characterization and modeling, and channel modeling for special scenarios.

**Jie Huang** (Member, IEEE) received the B.E. degree in information engineering from Xidian University, Xi'an, China, in 2013, and the Ph.D. degree in information and communication engineering from Shandong University, Jinan, China, in 2018.

From October 2018 to October 2020, he was a Post-Doctoral Research Associate at the National Mobile Communications Research Laboratory, Southeast University, Nanjing, China, supported by the National Post-Doctoral Program for Innovative Talents. From January 2019 to February 2020, he was a Post-Doctoral Research Associate at Durham University, Durham, U.K. Since March 2019, he has been a part-time Researcher at the Purple Mountain Laboratories, Nanjing. Since November 2020, he has been an Associate Professor with the National Mobile Communications Research Laboratory, Southeast University. He has authored and coauthored more than 40 papers in refereed journals and conference proceedings. His research interests include millimeter waves, massive multiple-input multiple-output (MIMO), reconfigurable intelligent surface channel measurements and modeling, wireless big data, and 6G wireless communications.

Dr. Huang received the Best Paper Awards from International Symposium on Wireless Personal Multimedia Communications (WPMC) in 2016, International Conference on Wireless Communications and Signal Processing (WCSP) in 2020, and WCSP in 2021. He has served as a TPC member for IEEE/China Institute of Communications (CIC) International Conference on Communications in China (ICCC) in 2017, 2018, and 2021, and delivered two tutorials in the IEEE/CIC in 2021 and the IEEE International Symposium on Personal Indoor and Mobile Radio Communications (PIMRC) in 2021.

**Jian Sun** (Member, IEEE) received the B.Sc. degree in applied electronic technology, the M.Eng. degree in measuring and testing technologies and instruments, and the Ph.D. degree in communication and information systems from Zhejiang University, Hangzhou, China, in 1996, 1999, and 2005, respectively.

From 2005 to 2018, he was a Lecturer with the School of Information Science and Engineering, Shandong University, Jinan, China. Since 2018, he has been an Associate Professor. In 2008, he was a Visiting Scholar with the University of California at San Diego (UCSD), San Diego, CA, USA. In 2011, he was a Visiting Scholar with Heriot-Watt University, Edinburgh, U.K., supported by U.K.–China Science Bridges: Research and Development on (B)4G Wireless Mobile Communications Project. His current research interests include signal processing for wireless communications, channel sounding and modeling, joint communications and sensing, maritime communication, visible light communication, and software-defined radio.

**Wensheng Zhang** (Member, IEEE) received the M.E. degree in electrical engineering from Shandong University, Jinan, China, in 2005, and the Ph.D. degree in electrical engineering from Keio University, Tokyo, Japan, in 2011.

He was a Visiting Scholar at the University of Oulu, Oulu, Finland, in 2010, and the University of Arkansas, Fayetteville, AR, USA, in 2019. In 2011, he joined the School of Information Science and Engineering, Shandong University, where he is currently an Associate Professor. His research interests lie in tensor computing, random matrix theory, and intelligent B5G wireless communications.

**Zhiquan Bai** (Senior Member, IEEE) received the M.Eng. degree in communication and information system from Shandong University, Jinan, China, in 2003, and the Ph.D. degree (Hons.) in communication engineering from Inha University, Incheon, South Korea, in 2007, under the Grant of Korean Government IT Scholarship.

From 2007 to 2008, he was a Post-Doctoral Researcher with Inha University. From 2015 to 2016, he was a Visiting Professor with The University of British Columbia at Kelowna, Kelowna, BC, Canada. Since 2007, he has been an Associate Professor with the School of Information Science and Engineering, Shandong University. His current research interests include cooperative and multiple-input multiple-output (MIMO) systems, visible light communications, cognitive radio networks, resource allocation and optimization, and 5G wireless communications.

**Kang An** is currently pursuing the Ph.D. degree with the Department of Electronic Information Engineering, Beihang University, Beijing, China.

From 2013 to 2018, he worked with the Beijing Institute of Mechanical and Electrical Engineering, Beijing. In 2019, he joined the Innovation and Research Institute of HIWING Technology Academy, Beijing, and in 2020 was a Senior Engineer. His research interests mainly include antennas and electromagnetics.

**Zengliang Li** received the Ph.D. degree from the School of Information and Electronics, Beijing Institute of Technology, Beijing, China, in 2010.

He is currently working as the Director of the Advanced Information Technology Center with the Innovation and Research Institute of the HIWING Technology Academy, Beijing. His current research interests include synthetic aperture radar, integrated radio frequency, and new system network communication technology.

**El-Hadi M. Aggoune** (Life Senior Member, IEEE) received the M.S. and Ph.D. degrees in electrical engineering from the University of Washington (UW), Seattle, WA, USA, in 1984 and 1988, respectively.

He is currently a Professor and the Director of the Sensor Networks and Cellular Systems (SNCS) Research Center, University of Tabuk, Tabuk, Saudi Arabia. He is listed as an inventor in several patents, one of them was assigned to Boeing Company, Chicago, IL, USA. He is a Professional Engineer registered in the state of Washington. He has coauthored articles in IEEE and other journals and conferences and served on editorial boards and technical committees for many of them. His research interests include wireless communication, sensor networks, power systems, neurocomputing, and scientific visualization.

Dr. Aggoune received the IEEE Professor of the Year Award from UW. He was the Director of the laboratory that received the Boeing Supplier Excellence Award. He served at several universities in the USA and abroad at many academic ranks including endowed chair professor.